

Project information

Project full title	Connecting Russian and European Measures for Large-scale Research Infrastructures – plus
Project acronym	CREMLINplus
Grant agreement no.	871072
Instrument	Research and Innovation Action (RIA)
Duration	01/02/2020 – 31/01/2024
Website	www.cremlinplus.eu

Deliverable information

Deliverable no.	D4.4 (D33)
Deliverable title	Scientific report on the conceptual development of the diagnostics system including the layout of the diagnostic system
Deliverable responsible	DESY
Related Work-Package/Task	WP4
Type (e.g. Report; other)	Report
Author(s)	Barabin Sergey V., Liakin Dmitry A., Orlov Andrey Y., Saratovskikh Michail S., Savchenko Alexander A., Tishchenko Alexey A., D.Yu. Sergeeva, Voinalovich Ye., Lepetyukha A., Suprun S.
Dissemination level	Confidential
Document Version	1
Date	2022/01/31
Download page	

Document information

Version no.	Date	Author(s)	Comment
1	2021/-1/30	Barabin Sergey V., Liakin Dmitry A., Orlov Andrey Y., Saratovskikh Michail S., Savchenko Alexander A., Tishchenko Alexey A., D.Yu. Sergeeva	



Table of Contents

1. Annotation	3
2 Characteristics of light sources and their diagnostic systems.....	4
2.1 Main beam parameters	4
2.2 Characteristics of ring accelerators.....	4
2.3 Characteristics of electron rings.....	5
2.4 Light Sources Characteristics	6
3 The USSR parameters and Main Ring Diagnostics Layout.....	7
4 Storage Ring Vacuum Channel EM Diagnostics.....	11
4.1 Beam Position Monitors.....	11
4.2 Current Transformers	16
4.3 Striplines	17
5 Gamma Ray Diagnostics	20
5.1 Beam Loss Monitors	20
6 Synchrotron radiation diagnostics	23
6.1 Retarded potentials	23
Time in the system	23
The first order approximation	24
Retarded field.....	25
Radiation from a point	25
Algorithms	27
Circles on the water.....	27
6.2 Transverse Profile and Emittance Measurement.....	28
6.3 Purity Monitor	45
6.4 Bunch Length Measurements	51
6.5 Halo Monitor	58
7 References.....	61
Addendum	67

Conceptual development of the diagnostics system including the layout of the



diagnostic system

1. Annotation

Diagnostics of an accelerated electron beam is a necessary part of an electronic synchrotron - a source of synchrotron radiation. Separate diagnostic systems, such as the beam position detection system, serve during the routine operation of the accelerator. Others are used for a more detailed and specific study of the properties of the beam to assess its quality and develop recommendations for improving various synchrotron systems. Thus, the design of a complex system of an electron accelerator-storage complex includes the development of diagnostic components already at the early stages of design. This document discusses the elements of beam diagnostics in relation to the future Russian synchrotron radiation source USSR. When performing the work, the European accelerator ESRF (Grenoble), which is close in class, was taken as a sample of the diagnostic system.

The text provides a general description of the systems with their main characteristics and comments on their possible improvement. The development of tools is described, both in terms of possible device models and in terms of software description of processes in optics, electrodynamics, etc.



2 Characteristics of light sources and their diagnostic systems.

2.1 Main beam parameters

The main beam parameters in the USSR light source storage ring are following: 1) beam intensity – beam current, or charge of bunches – for ring machines, this also makes it possible to determine the lifetime of the beam in the ring after injection; 2) beam energy, or speed of the beam; 3) the transverse position of the beam, by measuring which it is also possible to calculate the main characteristics of the storage ring, stabilize the beam orbit, and optimize the process of beam injection into the ring; 4) characteristics of the beam quality: a) compactness of the beam in transverse directions – transverse profiles; b) readiness of the beam for transportation through the vacuum channel of the storage ring, and also for light source experiments – beam emittance; c) characteristics of bunch patterns in the longitudinal direction – longitudinal profile and filling pattern; d) purity of the beam in the longitudinal direction – bunch purity; e) purity of the beam in the transverse coordinates – halo monitor; e) measurement of errors in beam dynamics – beam loss monitor.

2.2 Characteristics of ring accelerators

Ring accelerators, in contrast to linear ones, have the following distinctive characteristics [1]:

- A linear accelerator has many accelerating cavities through which the beam passes once. One can consider a linac as an ‘open loop’ system in the sense that there exists no possibility for orbit feedback, and everything depends on the start parameters. In contrast to that, a circular accelerator or storage ring has only a comparable small number of accelerating cavities. The same particles fly in the same orbit many times, and it is necessary to measure their multiturn parameters. It can be understood as a ‘closed loop’ system in the sense that there exists a periodical solution for the particle orbit, and orbit feedback is possible.
- Due to the closed loop behavior resonances can occur in the system. This must be taken into account when designing a synchrotron, and it is necessary to measure the characteristics of the storage ring to determine the conditions for the occurrence of resonances.
- A linac is a pulsed system. This means that the signals generated by the beam are a sequence of single events which may vary from shot to shot, the formation of an equilibrium state is not possible. A storage ring is a continuous wave (cw) system, the signals from the beam are repetitive and stable in general for many turns. It is possible that the beam reaches a kind of equilibrium state, and with it also the beam generated signals. Therefore, high precision can be achieved by averaging, and the signals are typically treated in the frequency domain.
- In a linac emittance and energy are functions of the location in the accelerator. In ring accelerators, emittance and beam current are non- or slowly varying parameters.



- In linac, because the charge can be lost everywhere in the machine, many devices for transfer measurements are required. In case of beam loss in the machine the gun will supply charge until it is stopped e.g., by an interlock. In storage ring, in case of a beam loss there are no particles in the storage ring until the beam is transferred again through the injector chain.

2.3 Characteristics of electron rings

The main difference in the requirements for diagnostics of electron accelerators from ionic ones is due to the differences in the electron mass as compared to the proton mass, which is three orders of magnitude less [1]. This leads to both different beam dynamics and different diagnostics requirements.

- In the storage ring of the synchrotron, the electron beam is completely relativistic (starting from energies of several MeV compared to 6 GeV in the USSR ring)
 - This means that it has a constant orbital frequency
 - The beam does not need to be accelerated by changing the intensity of the magnetic field in the bending magnets (but it is necessary to compensate for the beam energy loss due to synchrotron radiation)
- The electron beam in the storage ring has a high intensity of X-ray synchrotron radiation. The emission of synchrotron radiation has strong influence on both particle dynamics and beam diagnostics.
 - The emittance of the electron beam along the horizontal coordinate in the storage ring of the synchrotron is completely determined by the structure of the ring, and tends to an equilibrium value determined by the competing processes of radiation suppression and quantum excitation. The vertical emittance is defined by the coupling between both transverse planes and typically very small. Therefore, the beam emittance in the storage ring is determined by the ring itself and not by the injector chain, i.e., emittance blow-up is not critical and the injector chain has relaxed requirements. Accordingly, short-term excitation of the beam does not lead to an increase in the emittance, and it is possible to regularly measure the main characteristics of the ring: tune, chromaticity, and coupling.
 - Due to synchrotron radiation, the electron beam loses energy in the storage ring in accordance with the expression $\Delta E_y = 8.85 \frac{E^4 [\text{GeV}^4]}{\rho [\text{m}]}$, therefore, this energy loss must be compensated for by accelerating resonators in the storage ring.
The voltage across the cavity is inversely proportional to the square of the rms bunch length. Accordingly, a high cavity voltage implies smaller bunch lengths.
 - Synchrotron radiation, both visible or X-ray, can be used to diagnose beam parameters such as profile or emittance.
 - A huge level of radiation power is emitted from the beam which is deposited in the accelerator environment. Such a level may easily lead to the damage of components, i.e., sensitive accelerator components have to be protected from direct SR



illumination and cooling is required in places where the power is deposited. The heat load on accelerator components due to the high SR power becomes critical. Therefore, the accelerator together with the instrumentation has to be protected, and cooling is required in locations where direct SR illumination cannot be avoided.

- When the beam current changes, the thermal load on the ring structure also changes, which leads to a change in its characteristics and, consequently, to a change in other beam parameters (emittance, betatron frequency, etc.), which must be kept constant for experimenters. Therefore, it is necessary either to thermally stabilize the vacuum channel of the storage ring, or to stabilize the beam current. The beam current decreases after injection; therefore, it must be restored by periodic injection of the beam into the ring (top-up mode).
- Both equipment and maintenance personnel must be protected from radiation.
- The electromagnetic field from an electron beam is much shorter and more intense than from a proton beam:
 - The electron beam interacts much more intensely with the vacuum volumes of the storage ring, which can lead to its instability due to inhomogeneities in the channel. This instability must be reduced, either by decreasing the interaction of the beam with the ring, by carefully designing the structure of the vacuum volumes of the storage ring; either suppressing it with bunch-by-bunch feedback.
 - This interactions of beam with vacuum volumes of the storage ring limits the maximum beam current in the ring.
 - The signals from the beam sensors are much shorter, so you need to have faster electronics to process them, or take special measures to stretch the signal edges (downconversion to a lower frequency range).
 - The signals from the beam sensors are much more intense, therefore, measures must be taken to protect the electronics from overvoltage.

2.4 Light Sources Characteristics

The key parameter of a light source is the spectral brilliance B which is defined as follows [1]:

$$B = \frac{\text{Number of photons}}{[s][\text{mm}^2][\text{mrad}^2][0.1\% \text{ bandwidth}]} \quad (1)$$

Thus, B is a measure of the phase space density of the photon flux. The user requirement is to have a high brilliance which means as many monochromatic photons as possible emitted from a minimum source region on the sample. The brilliance can be rewritten as a function of the accelerator parameters in the following form:

$$B \propto \frac{N_{\gamma}}{\sigma_x \sigma'_x \sigma_y \sigma'_y} \propto \frac{I_b}{\epsilon_x \epsilon_y} \quad (2)$$

with I_b the beam current, and ϵ_x, ϵ_y are the horizontal and vertical beam emittance. According to that equation, there are two requirements for the accelerator to achieve a high brilliance:



- High beam current. This has the following implications for beam diagnostics:
 - To achieve the high currents, diagnostics is needed to detect and damp instabilities.
 - To cope with high heat load, heat load changes may lead to a position drift of accelerator and beam line components which the user will see immediately as a change in the photon flux on the sample.
- Small beam emittances. The implications are:
 - To achieve small emittances. The choice of the proper magnet lattice defines the minimum achievable emittance. Lattices in use are the Double Bend Achromat (DBA) or the Triple Bend Achromat (TBA), for example. However, this is a task for the lattice designer and will not be covered here.
 - To measure small emittances. If the accelerator is designed to have a small emittance, it is mandatory to have monitors which are capable of measuring this beam parameter. To measure the small transverse emittance in the storage ring, it is necessary to measure the small transverse dimensions of the beam with a high resolution.
 - To preserve the emittance. There are various effects resulting in emittance growth and with it a deterioration of the beam quality. Examples are fast beam orbit motions as well as short-term and medium-term component position drifts, i.e., stability is again a critical issue.

3 The USSR parameters and Main Ring Diagnostics Layout.

The determination of the requirements for the diagnostic system for the light source storage ring is based on the expected parameters of the beam, the requirements for its stability, the configuration of the storage ring, the configuration of the standard cell of the storage ring, and the scheme of beam injection into the ring.

The USSR 4th generation synchrotron radiation source has an electron energy of 6 GeV, and a beam current of 200 mA. To ensure the maximum brightness of the beam, it must have a horizontal beam emittance of the order of tens of pm.rad, with a vertical emittance about 5 pm.rad. Main USSR storage ring parameters are shown on Table 1.

Table 1. USSR Storage Ring Parameters

Energy:	6.00000 [GeV]
Beam Current	200 [mA]
Cell Number	40
Circumference	1103.15453 [m]
Revolution time	3679.72743 [ns] (0.27176 [MHz])
Betatron tune H	0.21000 (57.06958 [kHz])
Betatron tune V	0.34000 (92.39847 [kHz])
Momentum Compaction Factor	0.00007



Chromaticity H	+7.00000
Chromaticity V	+6.00000
Damping Partition H	1.51546
Damping Partition V	1.00000
Damping Partition E	1.48454
Radiation Loss	1992.28563 [keV]
Natural Energy Spread	8.51194e-04
Natural Emittance	7.15801e-02 [nm]
Radiation Damping H	14.62514 [ms]
Radiation Damping V	22.16385 [ms]
Radiation Damping E	14.92981 [ms]
Slip factor	-0.00007
Cavities Voltage	5000.00000 [kV]
Cavities Frequency	352.20000 [MHz]
Cavities Harmonic Number	1296
Synchronous Phase	2.73176 [rad] (156.51824 [deg])
Linear Energy Acceptance	5.01603 %
Synchrotron Tune	0.00341 (0.92792 kHz or 292.87 turns)
Bunch Length	3.23677 [mm], 10.79670 [ps]
Emitty from Dy	0.00000 [nm]
Emitty 1/gamma cone limit	0.01440 [pm]

The main tasks in beam diagnostics are to measure and stabilize its position, adjust the beam injection process, measure the beam current, and measure the beam emittance. The beam parameters and the location of the diagnostic equipment in the storage ring are primarily determined by the configuration of the standard cell of the main ring. Intermediate results on storage ring configuration are presented in *CREMLIN+ TASK 4.1 2020 report: Lattice and systems for the main ring* [2].

According to CREMLIN Task 4.1 report, the configuration of the USSR standard cell is similar to that of the ESRF EBS standard cell – hybrid multi-bend achromat lattice [3, 4].

The modernization of the lattice design of the storage ring of the ESRF EBS accelerator was carried out as part of the modernization of the 3rd generation synchrotron at ESRF to meet the requirements of the 4th generation synchrotron radiation source. The need to minimize the horizontal emittance of the beam leads to the need to increase the number of bending magnets (dipoles) in the cell from 2-3 to 7, in each of which the beam is rotated by a smaller angle than in the previous generation of synchrotrons, which leads to a decrease in the horizontal emittance of the beam in the storage ring. It was impossible to further increase the number of bending magnets in the section due to the fixed section size for the ESRF EBS accelerator.

A decrease of the bending angles leads to an increase in the strength of the sextupole magnets, which correct the chromaticity of the beam. This is difficult to implement and also leads to a decrease in the dynamic aperture, reduces the injection efficiency and the beam lifetime. Therefore, in the cell, 7 bending magnets (dipoles) are not evenly distributed: the distance between 2 pairs of outside dipoles (1st and 2nd, and 6th and 7th, dark blue on Figure 1) is greater than between the central ones (from the 2nd to the 6th). This allows to significantly reducing the strength of the



sextupole magnets located between the 1st and 2nd, and 6th and 7th dipoles. In the central part of the cell, there are four high-gradient horizontally focusing quadrupoles and three combined DQ bending magnets. Thus, the strength of the sextupole magnets decreases due to its increase in the magnets of the central part of the section, which is easier to implement.

The order of construction of the storage ring standard cell is as follows: 7 bending magnets with an increased distance between the two pairs of outside magnets to facilitate chromaticity correction; chromaticity correction sextupoles (green on Figure 1) and a pair of defocusing quadrupoles (red) around each are located between two pairs of outside dipoles; at the ends of the cell, and in front of the central dipole, there are fast correctors of the fast orbit correction system; and between all dipoles, sextupoles and correctors, as well as at the ends of the cell, the quadrupoles are located so that the arrangement of the magnets in the cell is alternately focusing-defocusing (FODO structure).

The equipment of the cell is located on four girders; the length of the cell together with the distance between the cells is about 27,5 m. The image of the ESRF EBS standard cell, with main types of magnets, correctors, diagnostics, and their distribution on supports, is shown in Figure 1 [5].

A decrease in the horizontal emittance in the USSR accelerator in comparison with ESRF EBS is achieved by increasing the number of cells in the storage ring from 32 to 40 [4]. A further increase in the number of cells in the storage ring is hindered by the need to increase the magnetic field strength in the chromaticity-correcting sextupole, which is difficult to implement, as well as a further decrease in the dynamic beam aperture, which complicates injection. Since the emittance value is inversely proportional to the cube of the number of cells, the horizontal emittance in the USSR storage ring decreased from 132 to 70 pm.rad. Accordingly, the total cell angle changes from 10° to 9°, and some changes in the power supply circuit and design of some magnets are required. Another cell option with an additional short magnet in the center of cell is also presented, increasing the cell length by 1.14 m, which can increase the number of beamlines from 34 to 74. The choice and implementation of injection scheme depends on the choice of the type of injector: a compact or full-size booster, or a linear accelerator with one of two types of electron source. The injection scheme can change from the off-axis injection scheme used in the ESRF EBS to any of the injection schemes with faster kickers and an additional straight section in the ring.

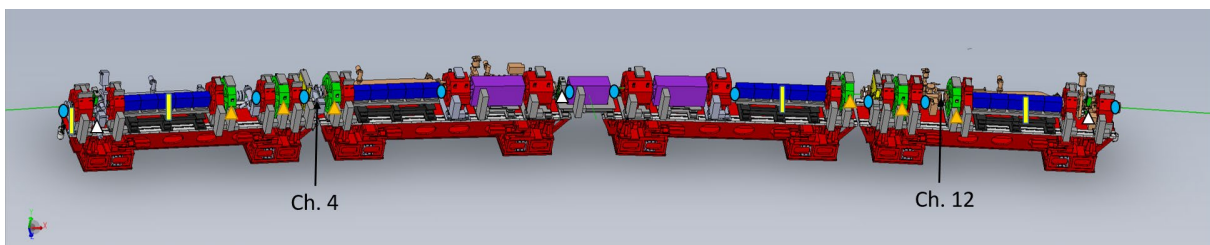






Figure 1. ESRF EBS standard cell, where  – Beam Position Monitor,  – Beam Loss Monitor,  – Fast Corrector,  – Slow Corrector.

The use of the same 352.2 MHz resonant frequency for the resonators compensating for the beam energy loss in the storage ring as in the ESRF EBS accelerator allows the use of the same



HOM-damped cavity driven Longitudinal Coupled Bunch Instabilities, which minimizes the need for longitudinal and transverse bunch-by-bunch feedback. However, since the bunch-by-bunch instability in the storage ring can arise not only in the resonators, then such a possibility should be provided. When optimizing the RF system for the USSR accelerator [6], a total accelerating voltage of 5 MV was chosen, which makes it possible to use 2 sections of five HOM-damped cavity 500 kV each instead of 3 in ESRF EBS, which frees one of the straight sections in the storage ring.

Thus, despite some changes in the USSR standard cell design compared to ESRF EBS, the ESRF EBS accelerator diagnostic system can be reviewed as the base diagnostic system for the USSR. Main types of the USSR Storage Ring diagnostics are shown on Figure 2.

- | | | |
|---|---|--|
| <ul style="list-style-type: none"> • Cell diagnostics: <ul style="list-style-type: none"> • 10 BPMs • 4 BLMs • Ch. 12 diagnostics: <ul style="list-style-type: none"> • Striplines • Current Transformers PCT+
FCT/ICT • 20-button BPM | <ul style="list-style-type: none"> • Ch.12 auxiliary devices: <ul style="list-style-type: none"> • Shaker • Scrapers <ul style="list-style-type: none"> • Horizontal • Vertical • Beam Inhibitor • Collimator | <ul style="list-style-type: none"> • Beamline diagnostics: <ul style="list-style-type: none"> • X-Ray Pinhole • Purity Monitor • Bunch Length Monitor • Vertical Halo Monitor • X-Ray BPMs |
|---|---|--|

Figure 2. USSR Storage Ring diagnostics.

USSR Storage Ring diagnostic devices can be classified according to its position on the storage ring and by types of measured fields. Additionally, some types of diagnostic systems exist in every cell, another only on several.

According to diagnostics devices placement and types of measured fields, it can be classified as: 1) devices, positioned on the Storage Ring vacuum channel and used electromagnetic fields to obtain diagnostic information from the beam; 2) diagnostic devices, placed on the beamlines and measuring synchrotron radiation of the beam, usually after bending magnets; 3) devices, placed outside the vacuum channel and measuring gamma rays to define beam loss pattern in the storage ring.

The layout of the diagnostic equipment and beam correctors in the standard cell of the storage ring is strongly determined by very small longitudinal space within cell (see Figure 1), and logically unchanged compared to ESRF EBS light source. Each standard cell contains 10 beam position monitors (BPM), 6 sextupoles with slow correctors, and 3 specialized fast correctors for the orbit correction system. To maximize signal values from the pickups, 10 BPMs should strive to be located in positions within cell with maximum beta values of the cell machine functions, compare Figure 1 and Figure 3.

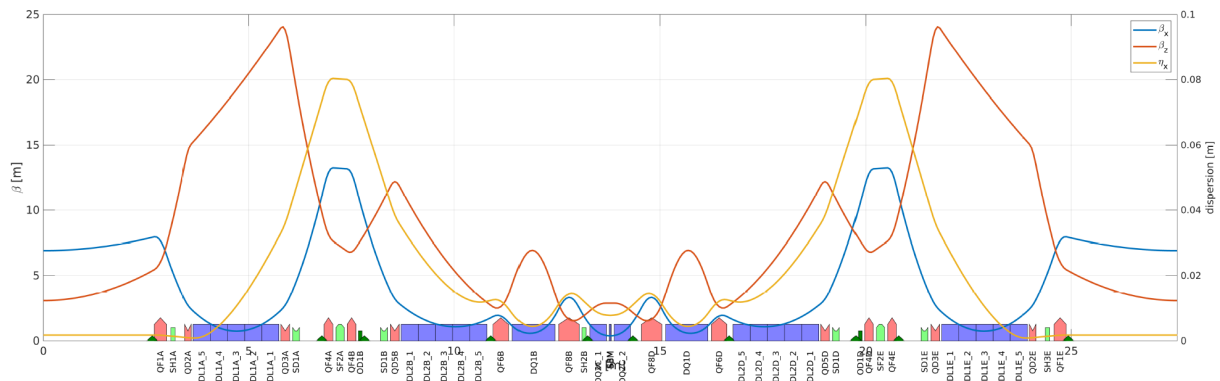


Figure 3. USSR storage ring standard cell machine function.

Other types of the vacuum channel EM fields storage ring diagnostics, such as: striplines, current transformers, special types of BPM, and several types of auxiliary devices, can be placed only on the two positions on the cell, noted on Figure 1 by the vacuum chamber number, namely CH4 and CH12.

In addition, there are four beam loss monitors (BLM) in each cell, three of these are placed near one of the bending magnets, and fourth – near beam entrance to the cell.

For the rest of the diagnostics and correctors, two positions are provided in the standard cell, after the corresponding sextupoles, indicated in Figure 1 as Ch. 4 and Ch. 12, where Ch is the number of the vacuum chamber in the cell. These positions can be used for such elements of diagnostics and corrector as: beam emittance monitors; beam current monitors; vertical and horizontal striplines and shakers, mainly used in bunch-by-bunch feedback, but can also be used for diagnostics; Visible Light Detectors and Bunch Purity Monitor; vertical and horizontal scrapers; collimators; beam inhibitors used in the interlock system. Each of these chambers should be modified differently for each diagnostic types. All electromagnetic diagnostic devices are placed on modified CH12. At the same time, some equipment for the synchrotron radiation diagnostic systems can be positioned both within CH4 and CH12 vacuum chambers. The addendum contains a table with the coordinates of the location of diagnostic devices along the storage ring.

4 Storage Ring Vacuum Channel EM Diagnostics

4.1 Beam Position Monitors

In the 4th generation synchrotron radiation sources, to increase the source brightness, it is necessary to maintain the stability of the beam orbit within 10% of its transverse dimensions. For the USSR accelerator, with expected values for horizontal and vertical emittances of 70 pm.rad and 5 pm.rad, respectively, the transverse dimensions of the beam are of the order of a few micrometers. Accordingly, beam position meters must provide sub-micrometer resolution for an orbit correction system.



The standard cell of the storage ring contains 10 beam position monitors (see Figure 1) – 2 at the entrance and exit of the section, 2 each around 2 chromaticity correction sextupoles, 2 at the entrance and exit of the central part of the section, and 2 around the central combined magnet in the middle of the section. Each device uses 4 capacitive sensors, the signal amplitudes from which depend on the beam current and the distance from the beam to the sensor. In a standard cell, two types of BPMs are used with capacitive sensor diameters of 6 and 8 mm (see Figure 4), depending on the cross-section of the beam transfer line at the location of the sensor installation. This is determined by shape of the lattice function in the standard cell, the β parameters of which are large at the edges of the section and small in the middle.

Detector Construction

The BPM design and their positions in the cell are well defined, their longitudinal size is limited by the dense arrangement of the magnets in the cell, and their operability and the ability to measure the position of the beam with the required accuracy have been tested on the EBS. For the cell option with an additional magnet in the middle of the cell, its machine function is slightly different, and if a decision is made to accordingly adjust the transverse dimensions of the vacuum chambers, the BPM design will also need to be adjusted accordingly, which can be done using tools such as BPMLab [7].

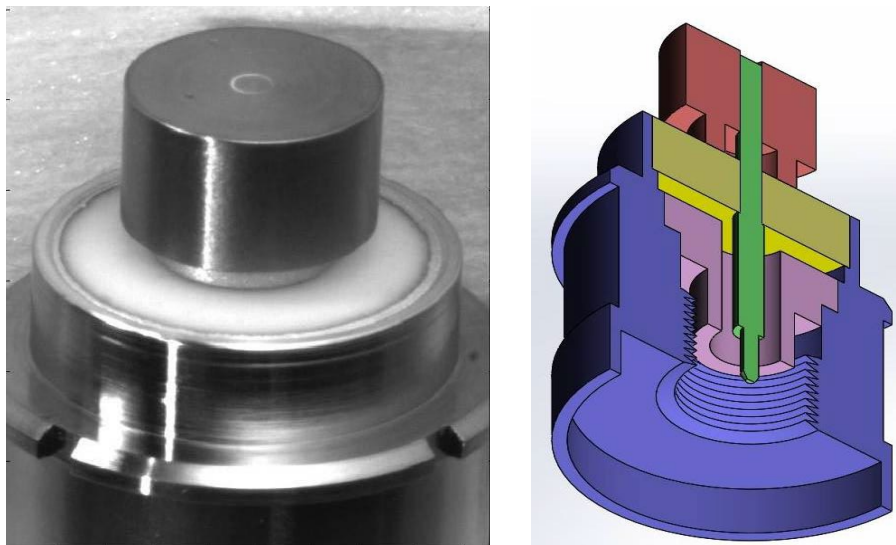


Figure 4. BPM button.

A variant of the classic design of a capacitive sensor is shown in Figure 4. Due to its small size, such a sensor is broadband enough to capture the first few harmonics of the electron beam current. The characteristics in the time domain also provide good separation of signals from neighboring bunches.

But even such a design can be improved when transferring it into USSR. The type of SMA connector used here implies the rotation of the cable assembly during the connection process. As a result, the central cores of both the cable and the sensor experience a torque load. Such a

connection is non-standard and is not recommended for operation.

Also, if one look at the sensor installed in the ion guide, one can note small gaps between the sensor electrode and the chamber wall. Such gaps are not justified by the electrodynamic requirements of the device, but greatly complicate the manufacture and assembly. Figure 5 shows the manufacturer's marks worth 250 Euros. At the same time, feedthroughs made from serial samples produced by established companies look quite acceptable.

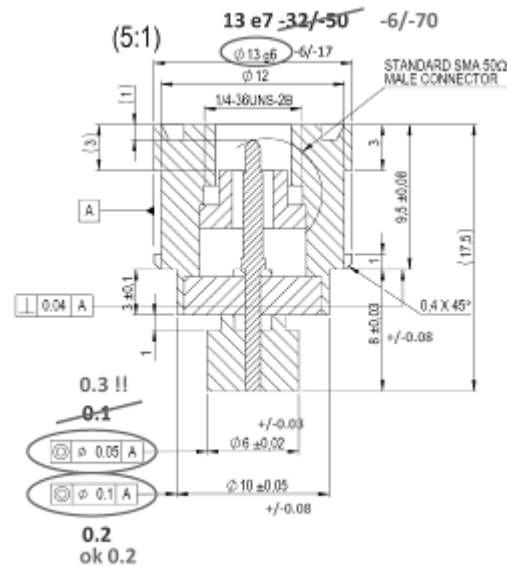


Figure 5. Sensor drawing with manufacturer's marks (Kees-Bertus Scheidt 2013)

Some inexpensive changes can be made to suppress possible unwanted resonances visible from the side of the accelerated beam.

Simulation

In modern times, the properties of objects and devices can be easily studied even before they are embodied in material objects. We have considered BPM using a FEM model with the geometry shown in Figure 6.

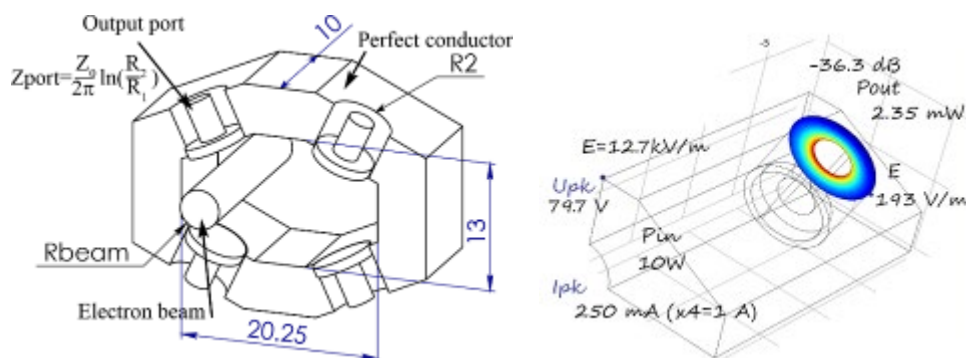


Figure 6. The geometry of the ion guide segment with installed beam position sensors. Some

simulation results

The task of detailed simulation, as a rule, is to identify patterns and derive a simplified model. The result of the calculation of the three-dimensional BPMN model can be considered an equivalent circuit from Figure 7, simple, but very accurately describing the properties of the sensor in the frequency domain.

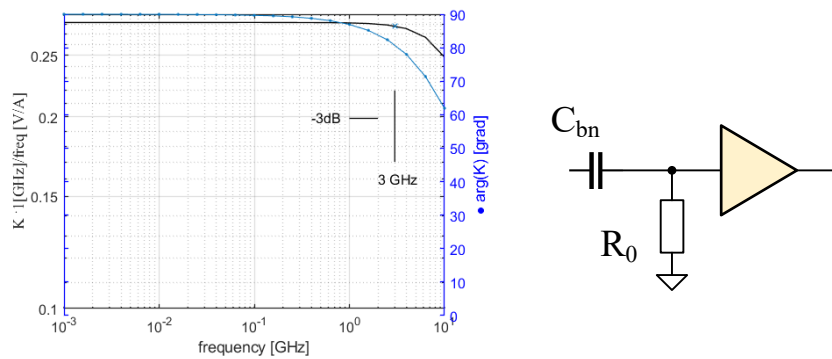


Figure 7. The transfer function normalized to the signal frequency. An equivalent scheme.

Also, the electromagnetic model can have different degrees of detail. Figure 8 represents a two-dimensional model of the BPM section used to analyze the transmission properties in the high frequency region. While waiting for the measurement signal, this characteristic may not be very useful, but it qualitatively shows the presence or absence of resonances that are undesirable in the beam wiring path.

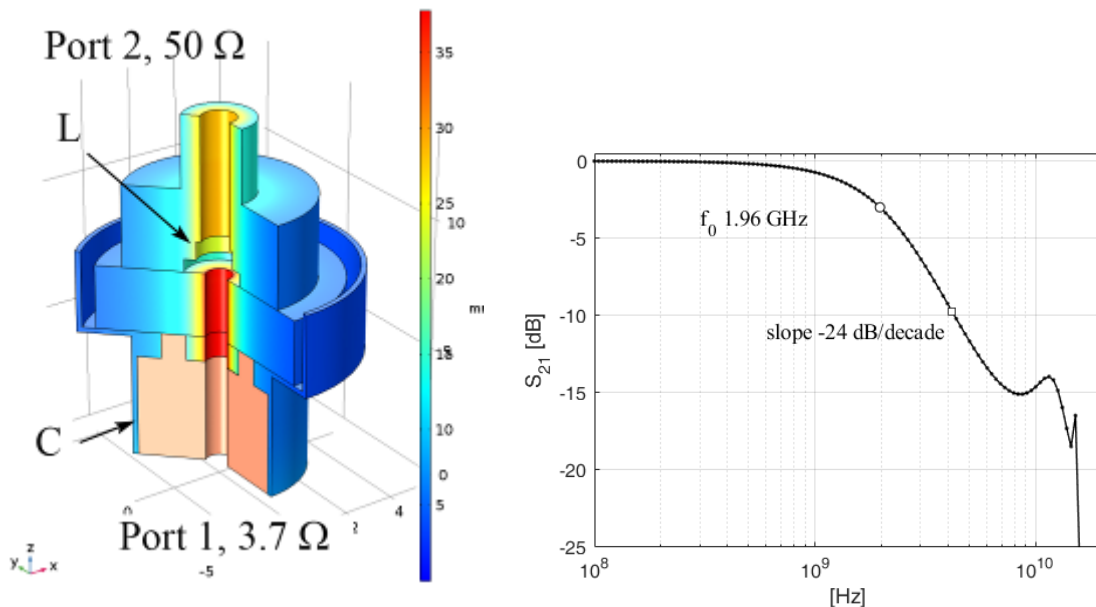


Figure 8. Detailed simulation of the button BPM section.

In addition to the frequency properties of the detector, we are also interested in knowing the relationship between the meter readings and the actual position of the particle beam. Practically, the

linearity of the BPM readings is achieved only with diagonally cut shoebox-type electrodes. The nonlinearity of the button-type electrode readings is shown in Figure 9.

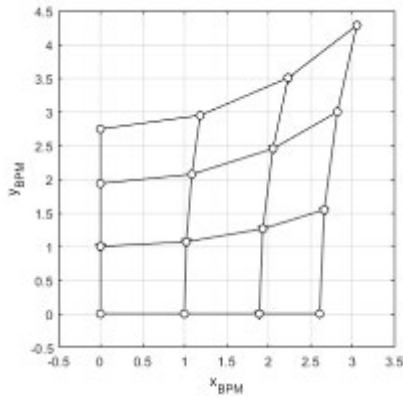


Figure 9. Calibration plot for the beam position

Electronics

Electronics for BPM looks quite traditional (see Figure 10). The beam current signal has a noticeable power and the preamp uses a low-noise (noise figure up to 2 dB) amplifier with a good dynamic range, input WSVR and a convenient power supply mode. As an alternative, an ultra-low-noise MIC is also considered, showing a noise factor of less than 1 dB due to a deterioration in coordination with the signal cable.

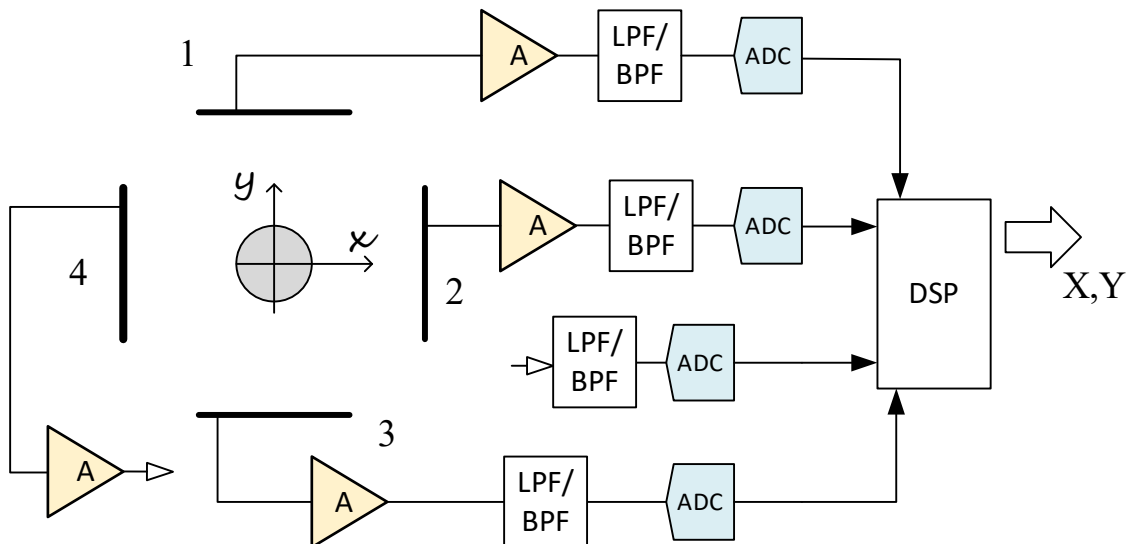


Figure 10. Front - end BPM electronics

The more detailed scheme not given here includes a range switch and signal path calibration circuits.

The data acquisition system from BPM sensors assumes the use of standard equipment for gigabit Ethernet. At the same time, high data transfer performance will be provided both by the data format and protocols, and by the performance of routing equipment.

4.2 Current Transformers

The beam current transformer will be installed in vacuum chamber CH12 in cells 5,10,15. We will use 3 types of current transformers:

- Fast Current Transformer (FCT) for filling pattern measurements
- Integrating Current Transformer (ICT) for measuring the charge of single bunches or macropulses for several filling patterns
- Direct-Current Current Transformer (DCCT), or Parametric Current Transformer (PCT) for measurements of average beam current

For all current transformer types, it will be used corresponding In-Air coils from Bergoz.

For FCT transformer, In-air FCT sensor from Bergoz [8] with higher upper cutoff frequency is preferable. It should be noted that for RF frequency 352 MHz, bunch length 11 ps and FCT sensor with 20 turns and 1.5 GHz upper cutoff frequency filling pattern can be distinguished, but longitudinal bunch profiles are strongly distorted.

The ICT transformer [9] lengthens the longitudinal profile of the very short pulses, thus making it possible to measure the parameters of the extended pulse (amplitude or area) and, accordingly, the charge or current of an individual bunch. This is possible by using two cores with winding within ICT sensor, with distributed capacitors on 1-st winding, where the fast bunch signal is stored and then slowly discharged into output load resistor, connected on second winding [10]. Usually, the selection of In-Air ICT sensor is trade-off between the sensor sensitivity, and maximum acceptable measured macropulse length. But for longest macropulse in the hybrid filling pattern, which is 40 RF bucket, or ~113 ns, ICT sensor with better sensitivity is almost acceptable. The ICT sensor is accompanied with Beam Charge Monitor electronics module, which allows to automate the process of measuring the bunch charge.

The DCCT sensor [11] is based on second harmonic measurements after saturation of two cores by modulating it by two sinusoidal signals of opposite polarities in kHz range [12]. It consists from In-Air DCCT sensor and electronic module within 19" 3U chassis, which generate modulated signals to sensor and convert measured signal to output DC voltage level.

Each replacement of CH12 chamber contain two types of current transformers: PCT and one of ICT or FCT. The scheme of chamber, developed in ESRF for EBS storage ring [5], is shown on Figure 11.



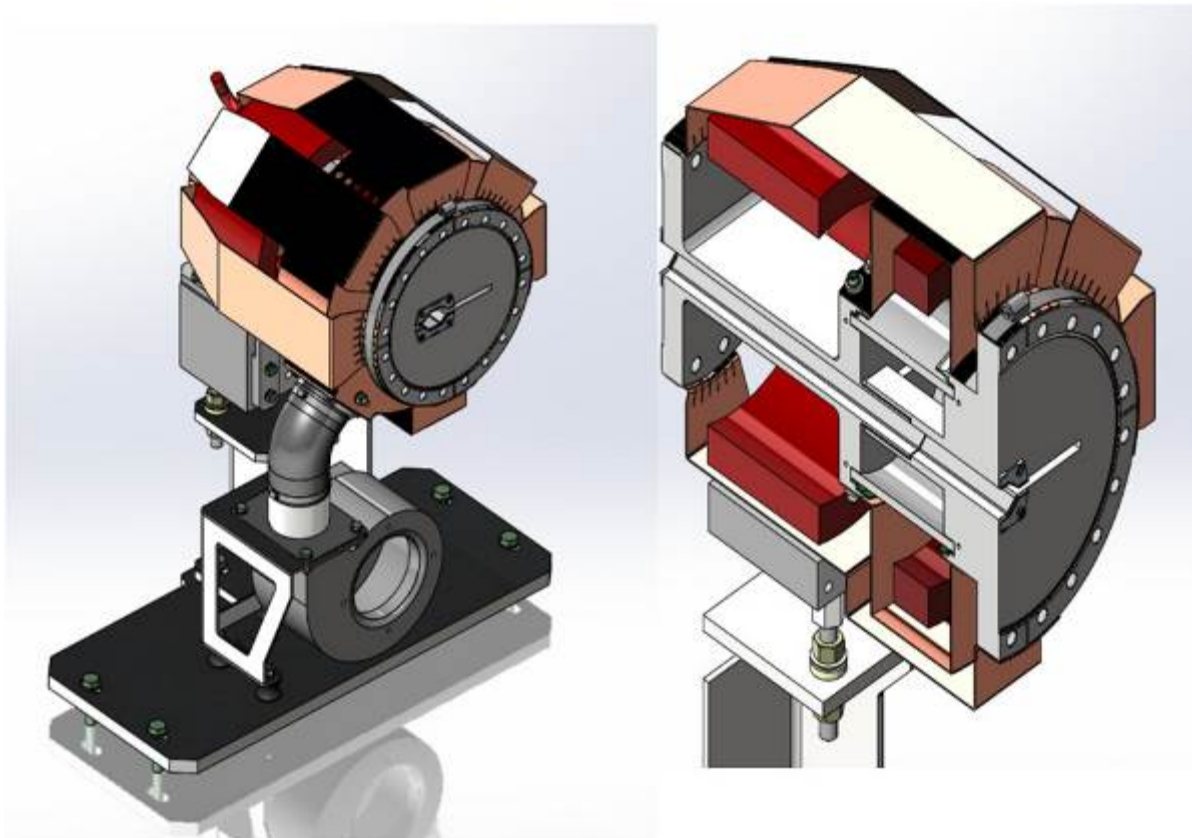


Figure 11. Current Monitors vacuum chamber.

Since the profile of the vacuum channel of the light source storage ring is not round, we cannot use standard in-flange sensors. Instead, we should use in-air sensors over self-made vacuum chamber. The measurement chamber is built over electron beam vacuum channel with required profile. The key point in camera design is to create gap in wall current of vacuum channel to prevent reverse wall current flowing, which in another case will mask beam current in both types of sensors. In current design these break under fast current transformer (ICT or FCT) is developed by composing vacuum channel from two overlapped tubes, left and right, and to fill space between tubes with ceramics. The design of that tubes was optimized for minimize radiation heating and to improve impedance budget. To improve vacuum inside vacuum channel additional ceramic tube around the gap was brazed/soldered on both flanges around the gap. Copper shielded case around fast current transformer protect external equipment from radiation through gap, but require external ventilation to prevent heating sensor damage. External large copper blades are used to wall current flowing around both current transformers.

4.3 Striplines

Three horizontal and two vertical striplines will be installed inside vacuum chamber CH12 within 5 different cells. It will be used for beam filling pattern measurement and, optionally, as beam

kickers in the vertical and horizontal planes of bunch-by-bunch feedback system.

All striplines has both an input and output port on each blade. Each of the striplines used in the feedback will be driven by a set of two 0.1 to 200 MHz bandwidth 100W solid-state power amplifiers.

Horizontal stripline will be used for filling pattern measurement because the sensitivity of such a pickup is high and allows to have a strong signal even at low current. For filling pattern measurements, only the input port is connected to the scope. The output one is connected to a coaxial cable terminated with a 50 Ω load in order to avoid undesired reflections. The signal coming out from the stripline is quite strong and has to be attenuated before being fed to the scope. A 30 dB attenuator was installed in the tunnel, close to the stripline port, and a second 10 dB attenuator was inserted before the scope. These attenuators also ensure that the signal acquired will not be polluted by reflection coming from bad mismatch between cables and the stripline or the scope ports.

The measurement stripline should be designed as quarter-wave couplers, because in that case the transfer impedance is maximum. Since the accelerating radiofrequency for the USSR storage ring is 352.2 MHz, which is equal to the frequency for the ESRF storage ring, and the striplines must be placed in the same vacuum chamber CH12, then the USSR can use the same stripline design that was developed for the ESRF storage ring.

The drawing of the ESRF's vacuum chamber CH12 with a horizontal stripline [5] is shown on Figure 12.

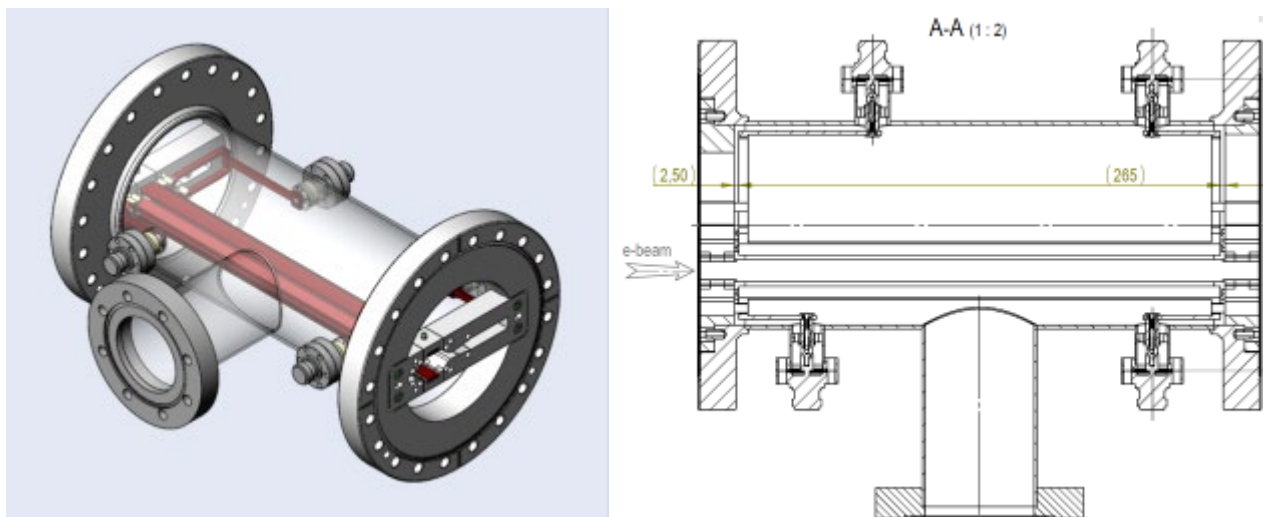


Figure 12. Horizontal Stripline.

The design of left and right blades of horizontal stripline is shown on Figure 13.

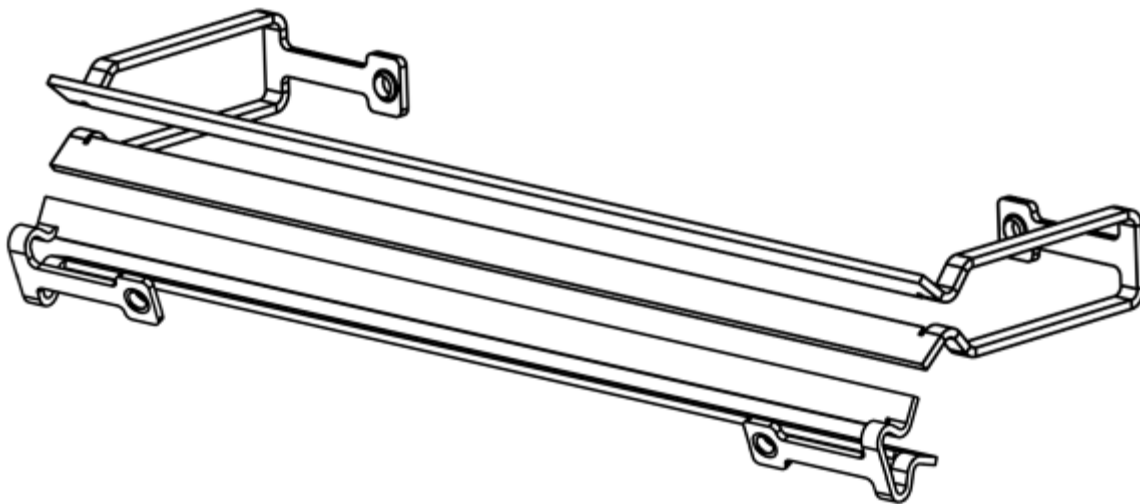


Figure 13. Horizontal Striplines.

The length of blades of horizontal stripline is 263 mm, which is close to quarter wave of 352.2 MHz accelerating frequency. The width of each blade is 9 mm, and its thickness is 2 mm. The characteristic impedance of each blade should match the characteristic impedance of two ports, i.e., 50 Ohm. It depends mainly from width of blade, distance between blades and walls of vacuum chamber, and coupling between stripline electrodes, and calculated same type as micro-strip line on the printed-circuit boards.

Stripline BPMs are well suited for short bunch observation because the signal propagation is considered in the design as for transmission-lines in microwave engineering. The azimuthal coverage of the stripline BPM can be larger than that of a button type yielding an increased signal strength [13]. Each stripline is a TEM transmission-line of characteristic impedance Z_0 . A stripline pick-up consists of a transmission line, having at both ends a feedthrough with an impedance of R_1 and R_2 matched to 50 Ohm. For bunch length in the USSR storage ring 11 ps, voltage signal from the stripline pick-up consist from two pulses of opposite sign, and profile of each pulse almost repeat longitudinal profile of bunch.

Vertical stripline contain two opposite blades on upper and lower sides of vacuum chamber CH12, 242 mm length, 14.4 mm width, 2 mm thickness each. The image of vertical stripline is shown on Figure 14.

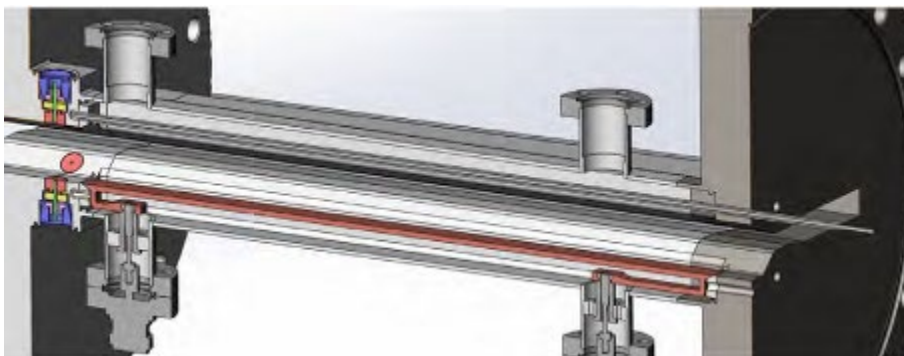


Figure 14. Vertical Stripline

A stripline geometry is usually employed for the transverse feedback kicker. Amplifier and kicker work in base-band, namely in the frequency range from $\sim DC$ to $\sim \text{frf}/2$. Figure 15 shows an example of a transverse feedback back-end adopting two power amplifiers feeding the downstream ports of two striplines in counter phase. The upstream ports are connected to $50\ \Omega$ power loads. Power low-pass filters can be optionally included to protect the amplifiers from peak voltages picked up by the kicker from the beam. [14].

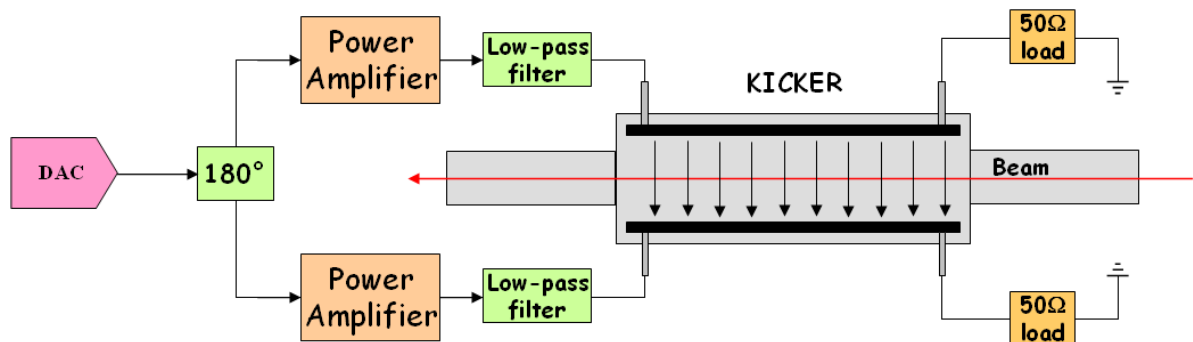


Figure 15. Stripline Kicker.

5 Gamma Ray Diagnostics

5.1 Beam Loss Monitors

Beam Loss Monitor system is used during normal operation to identify and locate partial beam losses that may be caused by the malfunctioning of various devices, vacuum leaks, unexpected obstacles, misalignment, and so on. BLM may be even more relevant during machine commissioning where this kind of problems are recurrent.

In general, the 3 most common causes of strong or excessive losses are:

- Aperture-limiting effects by e.g. a miss-aligned chamber, or a non-optimum trajectory of the injected beam. It is often after installation work in the ring, so directly at the restart after a shut-down period.
- A locally poor vacuum quality by e.g. a vacuum leak or a reduced conductance (e.g. a newly installed chamber with a different UHV pumping structure), or a poorly conditioned chamber (after its installation). Those are obviously occurring when such vacuum leaks develop, and usually soon afterwards confirmed by the increase of the pressure gauges in the affected zone.
- The characteristics of the electron beam itself (variations in dynamic aperture, resonances, Touschek scattering, etc.). These variations in the beam loss readings are directly correlated with other measurements on the beam's lifetime, emittance and injection efficiency.

BLM should cover a wide range of applications: measurement of fast and strong losses during injection is just as well possible as detection of very small variations of weak losses during the slow current decay.

Slow losses are unavoidable and are the one that determine the beam lifetime. They are usually confined in some hotspots and are due to the presence of collimators, scraper, septa, or other aperture limits. They also depend on the beam size and the population of the buckets, which lead to a deterioration of the Touschek lifetime. The typical time scale for slow losses is in the order of the second.

Fast losses are instead related with accidental effect, or some traumatic events such as perturbation due to injection. These losses can be distributed all around the machine, and can be visible on the single bunch or the single turn time scale.

Beam Loss Detectors Type Selection

The USSR is 6 GeV Light Source. The BLD has to detect losses generated by the 6 GeV electron beam.

When a high-energy electron is lost, it crashes on the vacuum chamber and creates an electromagnetic shower composed by electrons, positrons, and γ -Rays. In order to detect showers, a suitable plastic scintillator can be used to convert the energy deposited by particles into visible light, which can then be detected by a commercial PMT.

The detection of an electron loss can be affected by so-called Cherenkov radiators that are insensitive to the X-rays and gamma radiation. The visible light generated in such a radiator is caused by particles with mass only, which are also strongly present in the shower caused by a 6GeV electron loss. This type of detector could (in principle) have a significant advantage with respect to the so-called gamma scintillator in avoiding that additional external and heavy lead shielding.

The flux produced by the Cherenkov radiators was at least one order of magnitude below that of the EJ-200 scintillators (for comparable volumes). Also, the 2 mm thick lead shielding proved sufficient to be immune against the scattered X-rays, provided that (known) hot points of such scattering are avoided for the location of the BLD.

Consequently, it is no advantages of pursuing a Cherenkov based BLD since the (quartz) material is more expensive while less sensitive, and the only 2mm lead shielding has little impact on the size, weight and compactness of the final BLD.

Construction Characteristics, description of the principle of operation and design of the detector



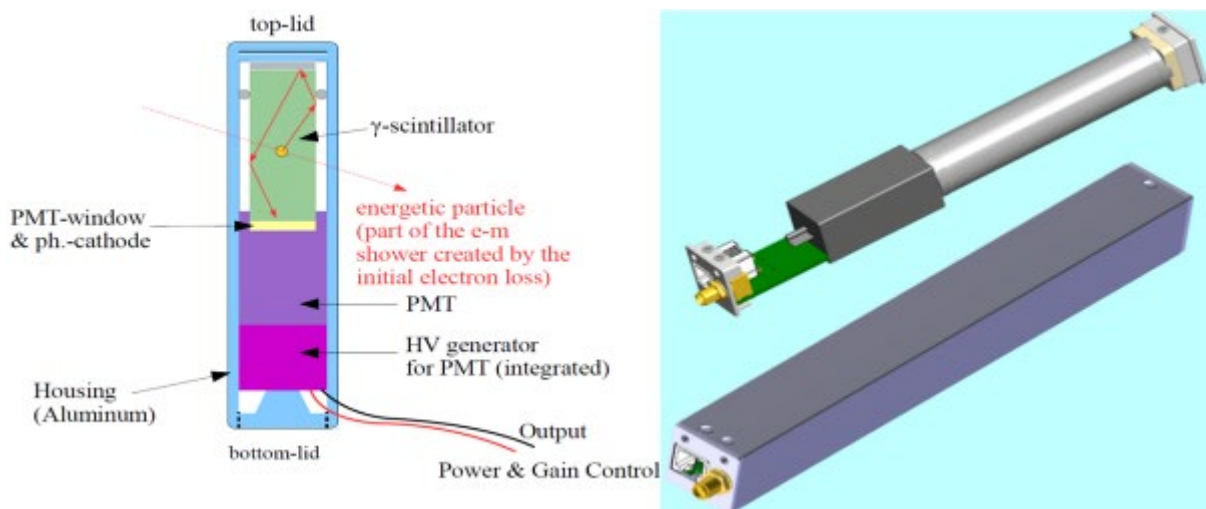


Figure 16. Beam Loss Detector.

A system consists of a detector head (BLD) and the electronics for signal acquisition and control (BLM). The BLD is compact, based on a scintillator coupled to a small photo-multiplier module. The BLM controls 4 independent BLDs and acquires data on different configurations of BLD prototypes.

BLD detector use a scintillator for the conversion of the products in the electro-magnetic shower (resulting from a crash of a 6GeV electron into the vacuum chamber etc.) into visible light photons, and to convert these photons into an electric signal by means of a photo-multiplier-tube (PMT).

A PMT coupled to the cylindrical rod of the scintillator. For the latter it is used EJ-200, which is an inexpensive plastic scintillator that is easy to handle and can also be machined to good optical quality. The sensitivity depends on the volume of the scintillator/radiator and then the efficiency of transmitting these generated visible photons to the photo-cathode of the PMT. The light produced in a cylindrical rod of 100 mm length and 22 mm diameter with a maximum possible efficiency to a window of only 8 mm needed a suitable adaptation, wrapped in reflective foil to minimize the light losses. It should be noted that the quality of the surface finishing of the 8 mm rod on the PMT side is very important.

The PMT module of Hamamatsu H10721-110 offered a satisfactory behavior in both modes of extreme uses like fast and strong losses (with the PMT connected to a 50 Ω impedance) and the slow and weak losses (now connected to a Hi-Z load). The H10721-110 device has an 8mm circular area of the effective photo-cathode. The 425 nm of peak-emission in the spectra of the EJ-200 scintillator is well suited for the photo-cathode characteristics of the PMT. The PMT requires to be powered by 5 V, and has a 0-1V control gain.

The PMT-scintillator system should be enclosed in a metallic casing, and an electronic card is needed to optimize PMT power supply, gain, and signal connections. The metallic casing is also sealed to provide a first ambient-light isolation. In order to minimize the background signal due to the synchrotron radiation scattered x-rays, each BLD is finally covered by a lead shielding. To obtain a

complete protection from ambient light, a “black hood” is added on top.

The main source of background for beam loss detection, using this particular BLD configuration, is represented by the scattered synchrotron radiation x-rays. The chosen scintillator is in fact sensitive both to charged particles and x-rays. To avoid false losses reading due to x-rays, the detector has been protected with a light lead shielding.

Tests for determining optimal lead thickness has been performed in ESRF using 2 or 3mm Pb shielding to protect the detectors. A strong dependence of the registered losses from the beam current is observed when using 2mm of lead. In this case the effect of the losses provoked by the scraping of the beam to reduce the current is comparable with the one measured in decay mode due to x-rays. This background is strongly attenuated when using one extra mm of lead. In this case losses due to the scraping are much stronger with respect to the background signal observed in decay mode.

These tests show that 3mm lead shielding is enough to reduce the background due to synchrotron radiation scattered x-rays.

6 Synchrotron radiation diagnostics

6.1 Retarded potentials

Time in the system

When using retarded potentials, it is important to correctly determine the coordinates of a particle at the moment it emits an electromagnetic wave. In general, the trajectory of a particle has a complex character, and the coordinates along the approximated curve are determined numerically.



$$\begin{aligned}
 |r - r_s(t)| &= ct_0 - ct \\
 r_s(t) &= R_{orb}(e^{j\omega t} - j) \\
 r &= ct_0 + x + jy
 \end{aligned}$$

$$\begin{aligned}
 |r - r_s(t)| &= ct_0 - ct \\
 r_s(t) &= \begin{bmatrix} R_{orb}\sin(\omega t) \\ R_{orb}(\cos(\omega t) - 1) \\ 0 \end{bmatrix} \\
 r &= \begin{bmatrix} ct_0 + x \\ y \\ z \end{bmatrix}
 \end{aligned}$$

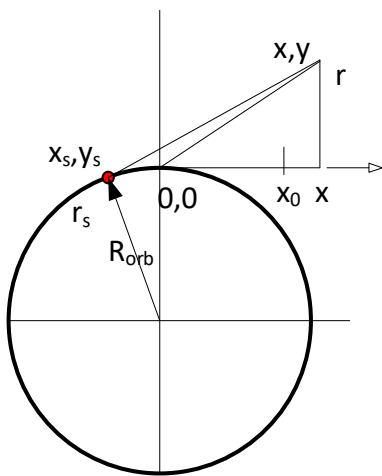


Figure 17. System variables.

The first order approximation

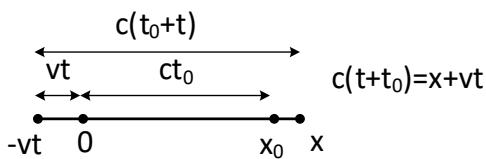


Figure 18. The first-order linearized system.

Now we can construct a function of the time of birth of an electromagnetic wave depending on the location of the observation point (see Figure 19). The emission time is postponed along the vertical axis of the three-dimensional graph. The two horizontal axes are the longitudinal and transverse coordinates. The graph clearly shows the formation of time compression caused by the Doppler effect. The spatial coordinates of the graph are measured in nanometers, which reflects the characteristic size of the observed effect.

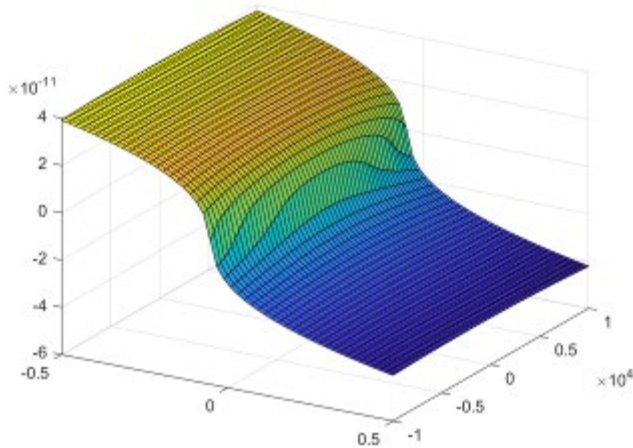


Figure 19. Time of emission as a function of coordinate.

Retarded field

Having determined the time of the moment of emission and the position of the particle, we can calculate the field in the area under consideration. For an electric field, the formula looks like:

$$E = \frac{1}{4\pi\epsilon_0} \frac{qn_s \times (n_s - \beta_s) \times \beta_s}{c(1 - n_s \beta_s)^3 |r - r_s|}, \quad (3)$$

where the values with the index s (source) refer to the moment of emission

Radiation from a point

An interesting case is the calculation of the field of a particle, emitted from one particular point of the orbit. In this case, the delay time is determined by the distance from the observation point to the fixed point of the particle location. Finding such a time does not require an iterative procedure and is found by direct calculation

$$t_s = \frac{|r - r_s|}{c} \quad (4)$$

The resulting instantaneous distribution of the field along the plane transverse to the direction of motion of the particle is shown in Figure 20.

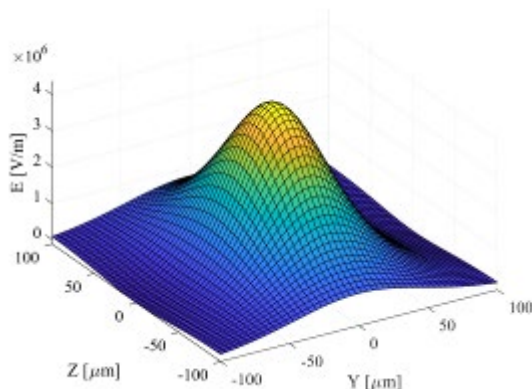


Figure 20. Instantaneous distribution of radiation intensity.

In practice, it is not possible to measure such a distribution, since it is difficult to separate electromagnetic radiation from one point from radiation emitted along neighboring sections of the trajectory. The method of retarded potentials makes it possible to reproduce the evolution of synchrotron radiation in time in such a way as it will be seen by a broadband detector installed at a distance. Figure 21 shows the calculation result in the time and frequency domains for a 6-GeV electron.

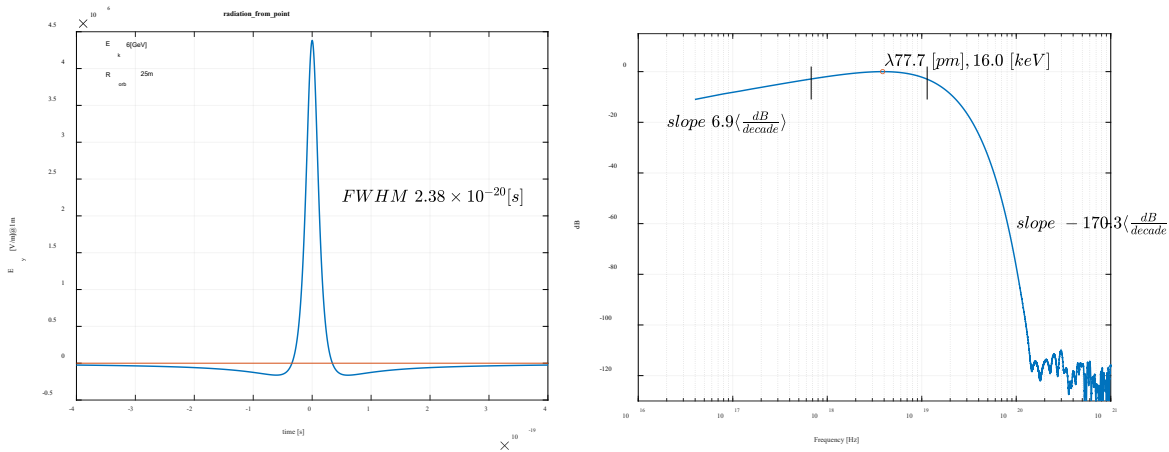


Figure 21. EMI pulse and its spectrum.

The calculation allows us to estimate the pulse duration on the detector and the frequency spectrum of radiation. Interestingly, the radiation power decreases sharply with increasing frequency and, on the contrary, slowly decreases in the long-wavelength range, which makes it possible to observe an electron beam in visible light.

As a useful application, it is possible to determine the region of the beam orbit from which the observer sees the radiation. Since in the course of solving the main problem we find the coordinates of the emitting particle, we can associate these coordinates with the output radiation.

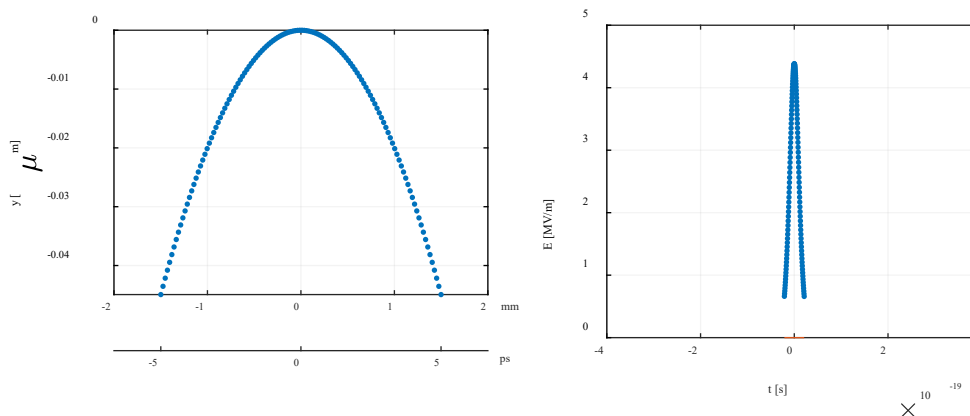


Figure 22. the trajectory of the emitting particle (left) and the emitted electromagnetic pulse along the tangent to the trajectory of the particle.

So, without taking into account the quantum nature of the radiation, Figure 22 shows that



the main radiation visible to the observer is formed on a section of the trajectory about 3 millimeters long. This size is important to know when using x-ray optics with a shallow depth of field.

Algorithms

The diagrams in 23 and 24 show the general sequence of calculations for obtaining the synchrotron radiation field in the area of interest to us. The input data for the calculations is the known trajectory of the particle and the grid of points in the three-dimensional region where the radiation is calculated. The trajectory can be set either by an analytical formula or in the form of a three-dimensional coordinate-time table in the general case. The velocity of a particle and its acceleration can be set in the same way.

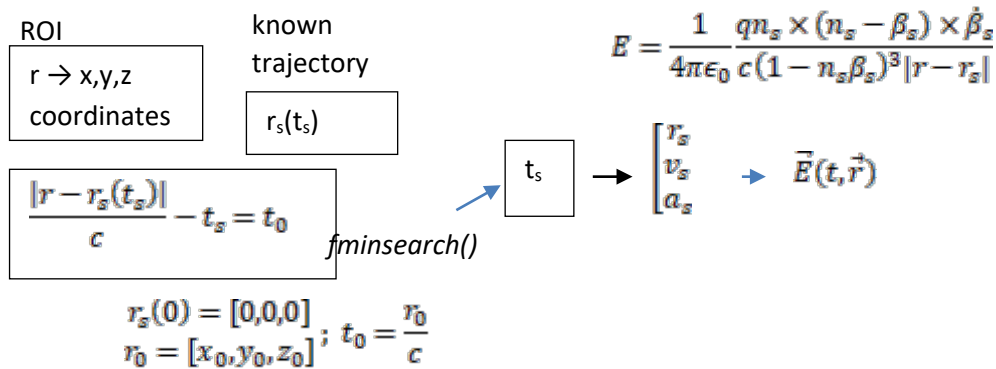


Figure 23. Algorithm for the problem solving in the laboratory coordinate system.

Usually, the trajectory is set in laboratory coordinates and when the coordinate system is changed, they and the time are additionally recalculated into the corresponding values. for a moving observer (Figure 24).

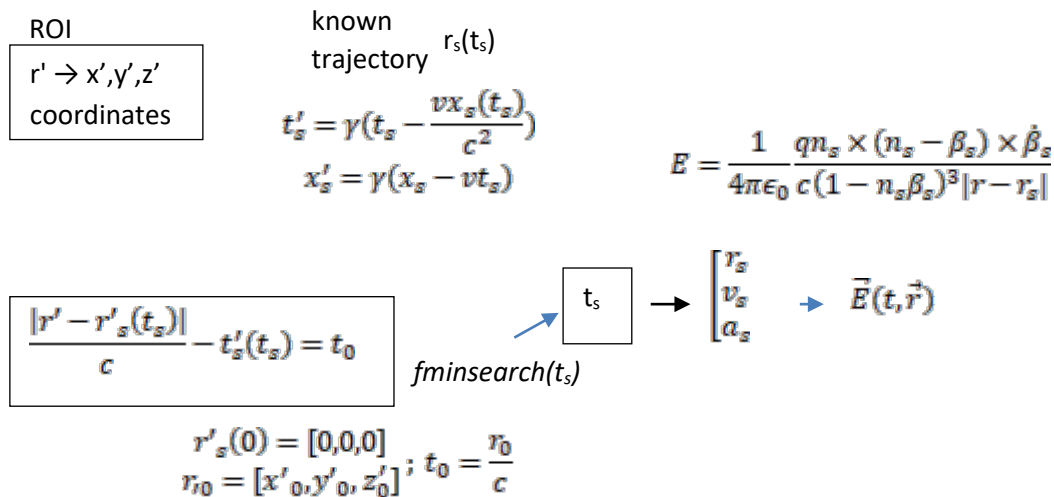


Figure 24. Solving the problem using laboratory time as a parameter.

Circles on the water

An effective way to demonstrate the operation of the algorithm is to visualize the



propagation of electromagnetic waves, shown in Figure 25. The figure shows circles diverging at the speed of light from an electron moving in a cyclic orbit. The difference in scales is clearly visible for the case when the observer is in a stationary coordinate system (on the left), and when the coordinate system moves with the velocity of an electron tangentially to its orbit. The marking of the axes on the graphs shows that the radiation region in the second case is much more compact and comparable to the wavelength of electromagnetic radiation. The wavelength can be determined roughly by the size of the area with compacted lines of equal time.

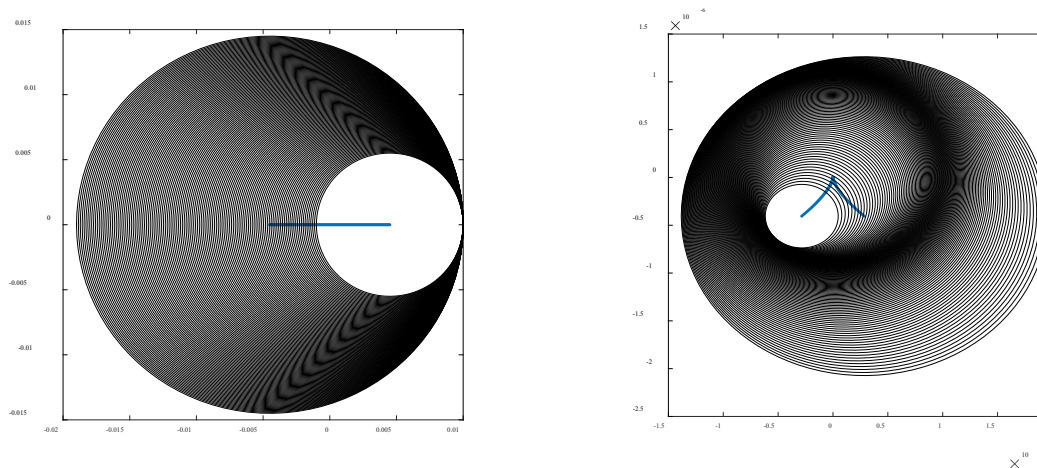


Figure 25. Ripple effect.

In the first case, the movement of the particle in the longitudinal and transverse directions differ by several orders of magnitude. The front of the electromagnetic wave propagating to the right is also very short compared to the size of the system. Due to such a difference in scale, the resulting solution for retarded potentials is difficult to adapt as initial conditions to the calculation by the finite element method. On the contrary, in the right figure, the longitudinal and transverse dimensions, as well as the length of the electromagnetic wave, are proportional to each other. Thus, it is clear that in a moving coordinate system, the various characteristic dimensions are much better matched.

6.2 Transverse Profile and Emittance Measurement

The spectral brightness of the radiation in the synchrotron depends on the beam brightness, which is directly proportional to the beam current and inversely proportional to the transverse emittance of the electron beam. Therefore, to increase the brightness of the source, it is necessary to control and reduce the emittance. This task is one of the most important now in the development and design of 4th generation sources.

At the moment, there are several ways to determine the transverse emittance, both direct measurements in phase space and indirect measurements. In a storage ring and for high-energy electrons, the determination of the emittance is basically reduced to measuring the transverse characteristics of the beam in real space, and then applying the theory of beam dynamics. These include, for example, a single measurement of the beam profile if the Twiss parameters are known; multiple measurements of the beam profile at different points of the trajectory, if the transition

matrix is unknown; quadrupole scanning method. The latter method is inapplicable in ring sources. The horizontal and vertical emittances are determined using the following relation [15]:

$$\sigma_i^2 = \beta_i \epsilon_i + (\eta_i \sigma_\epsilon)^2, \quad (5)$$

where σ_i is the measured beam size in the horizontal or vertical plane, respectively ($i = x, y$), β_i and η_i are the betatron and dispersion functions at the source point and in the corresponding plane; and ϵ_i and σ_ϵ are the emittance and the relative energy spread of the electron beam. Besides, there need knowing the matrix M , that is defined by the source construction. Then:

$$\begin{pmatrix} \beta_1 \\ \alpha_1 \\ \gamma_1 \end{pmatrix} = \begin{pmatrix} M_{11}^2 & -2M_{11}M_{12} & M_{12}^2 \\ -M_{11}M_{21} & M_{11}M_{22} + M_{12}M_{21} & -M_{12}M_{22} \\ M_{21}^2 & -2M_{21}M_{22} & M_{22}^2 \end{pmatrix} \begin{pmatrix} \beta_0 \\ \alpha_0 \\ \gamma_0 \end{pmatrix}, \quad (6)$$

where M_{ij} is the element of i -th line and j -th column of the matrix M , $\beta_1 \equiv \beta(z_1)$, $\beta_0 \equiv \beta(z_0)$ etc.

The multiple measurements method requires a minimum of three measurements of the beam size. Then, multiplying the left and right parts of eq. (6) by the emittance ϵ , and using the first line equation for three different points on the trajectory z_1, z_2, z_3 , one can find:

$$\begin{pmatrix} \epsilon\beta_1 \\ \epsilon\beta_2 \\ \epsilon\beta_3 \end{pmatrix} = \epsilon \begin{pmatrix} M_{11}^2 & -2M_{11}M_{12} & M_{12}^2 \\ N_{11}^2 & -2N_{11}N_{12} & N_{12}^2 \\ T_{11}^2 & -2T_{11}T_{12} & T_{12}^2 \end{pmatrix} \begin{pmatrix} \beta_0 \\ \alpha_0 \\ \gamma_0 \end{pmatrix} \equiv \epsilon R \begin{pmatrix} \beta_0 \\ \alpha_0 \\ \gamma_0 \end{pmatrix}. \quad (7)$$

The solution to this system is:

$$R^{-1} \begin{pmatrix} \sigma_1^2 \\ \sigma_2^2 \\ \sigma_3^2 \end{pmatrix} = \epsilon \begin{pmatrix} \beta_0 \\ \alpha_0 \\ \gamma_0 \end{pmatrix}, \text{ or } \begin{pmatrix} a \\ b \\ c \end{pmatrix} = \epsilon \begin{pmatrix} \beta_0 \\ \alpha_0 \\ \gamma_0 \end{pmatrix}, \quad (8)$$

where R^{-1} is the inverse matrix for R . To determine the emittance, it is necessary also to use the well-known relation between the Twiss parameters:

$$\gamma_0 = \frac{1 + \alpha_0^2}{\beta_0}, \quad (9)$$

Then from the solution (8) the emittance and the Twiss parameters follow:

$$\epsilon = \sqrt{ac - b^2}, \quad \beta_0 = a/\epsilon, \quad \alpha_0 = b/\epsilon, \quad \gamma_0 = c/\epsilon. \quad (10)$$

The method of a single measurement of the beam profile assumes that β -function of the source is known, its dependence on the coordinate z in the ring is determined by the elements of the transition matrix M , taking into account the cyclicity of electron motion. Then, as follows from relation (5), the emittance can be determined from the measured transverse size of the bunch at one



point of the trajectory.

Thus, the problem of determining the emittance is reduced to determining the transverse size of the beam. Therefore, a decrease in the emittance at 4th generation sources requires diagnostics of beams with small transverse sizes, which means that it is necessary to increase the resolution when determining the transverse sizes of the beam. For a horizontal emittance of 70 pm.rad and a vertical one of 5 pm.rad in the USSR storage ring, the transverse sizes of the beam are about several μm , depending on the β -function value on the synchrotron radiation source point. In some cases, destructive methods can be used in the synchrotron ring or in straight sections, such as luminescent or other screens or wire scanners, but for long-term beam monitoring, non-destructive diagnostic methods are predominantly used, for example, monitors based on residual gas ionization or monitors based on synchrotron radiation. Methods based on synchrotron radiation are classified as non-disturbing, and there are several options for using synchrotron radiation. The most common and reliable are the X-ray camera obscura, or pinhole camera [16] and interferometry [17, 18, 19], which is based on the analysis of the spatial coherence of radiation.

A standard tool for the beam transverse profile measuring is a pinhole camera system (Figure 26) [16], which used synchrotron X-ray radiation after bending magnets to measure beam size. This system records X-ray radiation from a dipole that has passed through a pinhole on a scintillator with a CCD video camera, and increase the size of the image of synchrotron radiation on the scintillator according to the following relation: $M = D/d$, where M is pinhole magnification factor, d is distance from radiation source to pinhole, and D is distance from pinhole to scintillation screen.

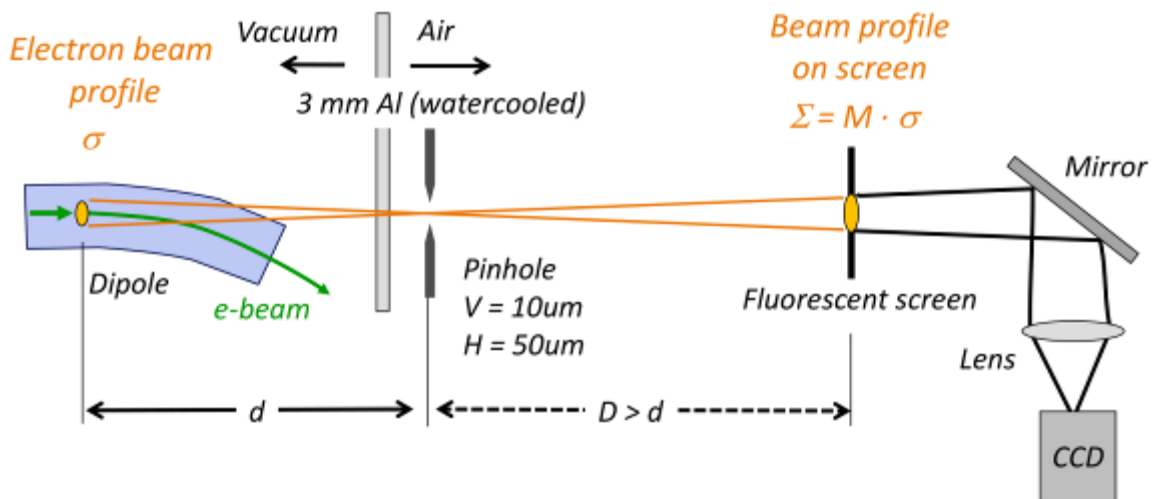


Figure 26. X-Ray Pinhole beam profile meter.

Synchrotron Radiation

Main bending magnet synchrotron radiation characteristics important for emittance measurements resolution are its spectral distribution and an opening angle of the vertical intensity profile. The fundamental limit of the beam size measurements is given by Heisenberg's uncertainty relation which can be reformulated as [21]:



$$\Delta\sigma = \frac{\lambda}{2\Delta\psi}, \quad (11)$$

where $\Delta\sigma$ is the resolution broadening due to diffraction, λ is synchrotron radiation wavelength, and $\Delta\psi$ is the opening angle of the emitted photon. While the horizontal emission angle is large due to the particle motion on a curved trajectory in this plane in a bending magnet, the vertical one is small and thus imposing the fundamental resolution limit.

There is a set of specialized computer codes for synchrotron radiation calculation and ray tracing, such as SRW [22], SPECTRA [23] or RAY [24], and a set of user interfaces for these codes, such as XOP [25], ShadowOui [26] or Ray-UI [24], but more important synchrotron radiation Characteristics can be estimated analytically. According to [27], the normalized spectral power density of synchrotron radiation can be described as:

$$\frac{dP}{d\omega} = \frac{P_s}{\omega_c} S_s\left(\frac{\omega}{\omega_c}\right), \quad (12)$$

where S_s is a dimensionless function that depends only on the ratio between the frequency ω and the critical frequency ω_c ; and the critical frequency ω_c is:

$$\omega_c = \frac{3c\gamma^3}{2\rho}, \quad (13)$$

where γ is beam Lorentz factor, and ρ is bending radius. The critical frequency ω_c divides the total power spectrum into two equal parts, and spectral function has maxima somewhat below the critical frequency.

The metal window in the vacuum chamber, through which the X-ray synchrotron radiation enters the pinhole, works as a high-pass filter, thus increasing the frequency value with the maximum radiation amplitude in the spectrum, and reducing the radiation intensity. Since this filter improves measurement resolution with radiation wavelength decreasing, but increase radiation detector error with radiation power decreasing, there is trade-off between them, which should be adjusted by regulating filter parameters with additional external copper absorber with variable thickness.

According to [28], an opening angle of the vertical intensity profile is:

$$\theta_{BM} = 2\sigma \simeq \frac{1}{\gamma} \left(\frac{\omega}{\omega_c}\right)^{-0.425}, \quad (14)$$

where σ is rms value of the Gaussian fitting the angular profile.

Pinhole PSF

The image profile recorded on the detector contains contributions from the magnified source image, the point spread function (PSF) of the pinhole, and the PSF of the detector system [15]. The



measured rms size of the image, Σ , is:

$$\Sigma^2 = (M\sigma_i)^2 + \sigma_{pinhole}^2 + \sigma_{detector}^2, \quad (15)$$

where σ_i is the electron source size, M is the magnification factor, $\sigma_{pinhole}$ is the rms size of the pinhole PSF, and $\sigma_{detector}$ is the detector rms resolution. Accordingly, the transverse size of the electron beam σ_i can be calculated by measuring the size Σ of the synchrotron radiation on the scintillator, and preliminarily calculating the pinhole PSF $\sigma_{pinhole}$ and experimentally measuring the detector PSF $\sigma_{detector}$.

The pinhole PSF can be decomposed by two parts:

$$\sigma_{pinhole}^2 = \sigma_{diff}^2 + \sigma_{aperture}^2, \quad (16)$$

where σ_{diff} is the size contribution from the diffraction of the pinhole, and $\sigma_{aperture}$ is the geometrical contribution due to the finite size of the pinhole. The contribution of the diffraction can be estimated analytically as

$$\sigma_{diff} = \frac{\sqrt{12} \lambda D}{4\pi A}, \quad (17)$$

where A is pinhole aperture. The geometrical projection size of the pinhole is given by

$$\sigma_{aperture} = \frac{A (D+d)}{\sqrt{12} d}. \quad (18)$$

As we can see, as the aperture increases, the geometric part increases, while the diffraction component decreases. Accordingly, we can define the optimum aperture that minimize the point spread function as

$$A_0^2 = \frac{12 \lambda d D}{4\pi (d+D)}. \quad (19)$$

For transverse beam size of several μm pinhole PSF contribution is dominant in image size on scintillator, and should be calculated very carefully. As it was shown in [15] and in [29], this analytical approximation is acceptable on beam sizes larger than $\sim 20 \mu\text{m}$. For smaller beam sizes, both optimum aperture determination and pinhole PSF contributions should be calculated from near-field Fresnel diffraction numerical simulation, calculating diffraction profile of a one-dimensional slit, as it shown in [30]. Thus [29], for beam size $\sim 5 \mu\text{m}$ pinhole PSF contribution on the scintillator is two times larger than magnified transverse beam size, what is about two times smaller compared with analytical approximation.

Emittance measurement system design for the USSR storage ring

As we can see from equation (5), to improve measurement system resolution, synchrotron radiation source point should be positioned on the minimum dispersion function and on maximum



beta function values. Observed the USSR storage ring standard cell machine function (Figure 3), we can find several bending magnets points with minimum dispersion function values: DL1A_5, DQ1B and DQ1D. Points DL1A_5 and DQ1D, which are also synchrotron radiation sources for beamlines, are defined as acceptable for x-rays radiation sources. Main storage ring parameters for DL1A_5 synchrotron radiation source is: bending magnet power 0.45 T and bending radius 44.1 m; $\beta_x = 1.0$ m, $\beta_z = 17.6$ m, $\eta_x = 4.9 \cdot 10^{-3}$ m, $\sigma_\epsilon = 0.011$. And same parameters values for DQ1D source are: $B=0.48$ T, $\rho = 41.5$ m, $\beta_x = 1.27$ m, $\beta_z = 3.94$ m, $\eta_x = 9 \cdot 10^{-3}$ m, $\sigma_\epsilon = 0.017$.

Accordingly, one channel of emittance measurement system, as it shown on Figure 26, consists from: x-ray synchrotron radiation source on bending magnets DL1A_5 or DQ1D; vacuum chambers with output window for x-ray radiation, which should include special crotch absorber that limits the horizontal angle of X-ray radiation to 0.5-0.6 mrad, reducing radiation heating and radiation dose to the output window; these vacuum chamber should be placed after bending magnets, replacing vacuum chamber CH4 or CH12; 3-mm water cooled aluminum window from vacuum chamber, worked as high-frequency filter for X-ray synchrotron radiation; additional vertically adjustable wedge-shaped copper absorber, which allows you to adjust the characteristics of the spatial high-pass filter; in-air 20x20 μm pinhole, formed by pairs of tungsten plates with aluminum inserts between them placed close to vacuum chamber [16, 31] on ~ 4 or 5 m from source points, with N_2 flushed pipe, to save pinhole aperture value; scintillator on 15-20 m from pinhole near storage ring wall, dependent from the storage ring building construction; scintillator material can be selected one of several: YAG:Ce – Bicron or LuAg:Ce, about several hundred μm thickness; mirror and lens assembly, to protect video camera from X-ray radiation; high-resolution CCD VCD, recording image from scintillator and transmitting it to one of digital host of control system.

Synchrotron radiation beam size measurement methods have significant resolution limitations, and as the emittance decreases, their improvement is required. In recent years, such work has been carried out, see, for example, studies at the ALBA synchrotron [32], where it is proposed to use rotating screens with double pins to measure the transverse beam sizes up to 2 μm .

In addition to synchrotron radiation, other types of radiation are being considered for use in beam profile (emitter) monitors. Thus, in the linear sections of the source for determining the transverse sizes of the beam, monitors based on transition radiation have proven themselves well, which, however, are destructive [30, 31]. Transition radiation is excited when electrons cross the target. The substance is dynamically polarized under the action of the Coulomb field of electrons and radiates. The effective emitting region depends on the transverse size of the beam; the theory for transition radiation is well developed, for both X-ray region and visible range, so the reconstruction of the transverse sizes is possible with high accuracy.

For example, in the extracted line of the SPring-8 synchrotron (Japan), six monitors based on optical transition radiation are used to determine the emittance. They are located at a distance of 2.65 m from each other along the beam trajectory [32]. The method has been tested for electrons with the energy of 1-8 GeV. The measured values of the horizontal emittance were 32 ± 5 nm · rad and 200 ± 29 nm · rad for the energies of 3 GeV and 8 GeV, respectively.



Similar experiments were carried out at Diamond facility for an electron beam with the energy of 3 GeV when the beam was transferred from the booster to the storage ring [36]. The main idea is still the same: measurement of the transverse size of the bunch at three different points of the trajectory, but with a single beam passage through three or four monitors based on optical transition radiation. The emittance measured in this way was 162 nm·rad. The results agreed well with the value determined by the quadrupole scan method.

Transition radiation is also used in another method for determining the emittance: a solenoid changes the beam size, i.e. on one screen (target), the size of the effective radiating region changes three times. This method is used for electrons with the energy about 4-5 MeV, which corresponds to diagnostics in the accelerator sections closest to the injectors; however, conceptually, nothing prevents the use of this method with three dimensions of the transverse size for other energy ranges as well. Transition radiation monitors mainly use aluminum or mylar targets, sometimes crystals [37].

Monitors using other types of radiation, for example, diffraction radiation and Smith-Purcell radiation, can serve as a non-disturbing analogue of transition radiation monitors. By nature and some characteristics, these types of radiation are close to transition radiation, but they are non-destructive schemes, since when the radiation is excited, there is no direct interaction of electrons with the target substance. Diffraction radiation is excited during the passage of electrons near the target, which has an inhomogeneity in the direction of electron motion. Smith-Purcell radiation is a particular case of diffraction radiation when the inhomogeneity is periodic. The use of these types of radiation for diagnostics is not as widespread as transition radiation, but research is currently underway to develop and test these schemes [38].

In the discussed methods, the problem independent measurement of the vertical and horizontal emittances arises, i.e. separate measurements of vertical and horizontal sizes of the beam, which, in the general case, are related. This problem was investigated for emittance diagnostics using optical transition radiation monitors [39], though for electrons of not too high energy (17–110 MeV), but, again, there are no fundamental energy restrictions for the applicability of this method. The solution to separate determination of the two transverse sizes is to use different polarizations of the transition radiation.

Using the interferometry in synchrotron radiation, this issue was considered in [40]. Simultaneous independent measurement of two transverse sizes becomes possible due to the use of four or five slits shifted relative to each other. In practice a fundamentally feasible idea is complicated by the lack of a consistent theory, which is needed to extract sizes from the measured interferograms, or by the arising the effect of polarization on the radiation pattern, etc.

Promising diagnostic method under development

Similar ideas of independent measurement of transverse sizes can be implemented using diffraction radiation or Smith-Purcell radiation. These types of radiation are most efficient for ultrarelativistic particles, since the effective emitting region is determined by the relation between the beam impact parameter h , vertical size of the beam σ and the effective distance at which the



Coulomb field acts $r_{eff} = \gamma\beta\lambda/2\pi$, with γ being the Lorentz-factor of the electrons, λ being the wavelength of radiation, $\beta = \sqrt{1-\gamma^{-2}}$, see fig. 1. For ultrarelativistic electrons we have $\gamma \gg 1$, that means that r_{eff} is high, and if the bunch size is small, then the high-energy beam is easier to position over the target.

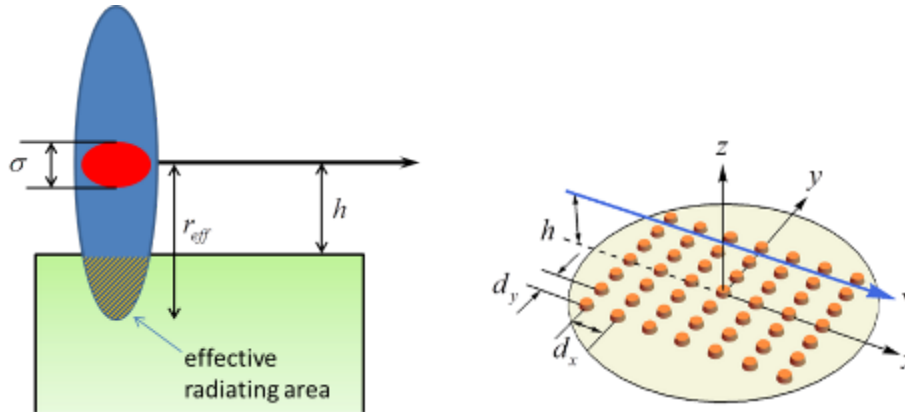


Figure 27. (left) Scheme of excitation of diffraction radiation by an electron beam; (right) scheme for excitation of Smith-Purcell radiation from a two-dimensional array of particles

As was shown in [41, 42], for a beam with the electron distribution inside closing to Gaussian, the vertical size in the expressions for the radiation intensity presents as σ/h . In the general case, the geometry of emitting of diffraction radiation (and Smith-Purcell radiation) is asymmetric with respect to the vertical size, and the dependence of the intensity on it is well known and analytically simple, which makes it possible to distinguish it from the horizontal size.

Asymmetry in the horizontal direction can be created due to the inhomogeneity of the target in the direction perpendicular to the beam motion. For example, a two-dimensional or three-dimensional array of metal or dielectric particles can act as such a target. Figure 27(right) shows an example of a two-dimensional point target [43]. In contrast to the usual target for Smith-Purcell radiation, the angular distribution contains additional maxima, the angular and spectral positions of which can serve as additional information for determining the horizontal size of the beam, see Figure 28.

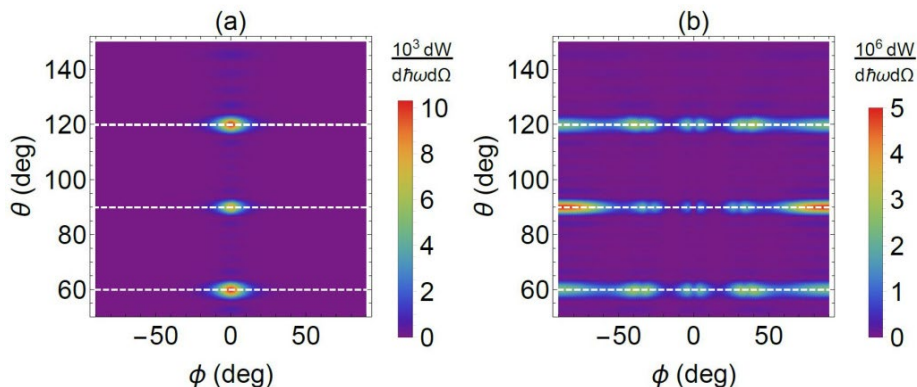


Figure 28. Angular dependence of the spectral-angular distribution of the Smith-Purcell radiation (a) for a conventional grating, (b) for a dotted target.

As mentioned above, in order to extract information about beam sizes, a well-developed radiation theory is needed. Such a theory for the target shown in Figure 27 (right) is developed based on the dipole approximation. Expressions for the radiation field and the spectral-angular distribution of the radiation energy were obtained in [44] for the normal flight of an electron over an array of particles.

The constructed theory was tested experimentally with the electron beam with the energy of 8 MeV at the LUCX facility, Japan [45]. The experimental results show good agreement with the theory. In practice, there is a spread of velocities in directions inside the beam, which was taken into account in [46], where the radiation field and the spectral-angular distribution of the radiated energy were calculated, and the angular positions of additional maxima were determined for an arbitrary orientation of the electron trajectory over the target.

The radiation intensity in the near zone was also calculated, see [47]. Despite the development of the theory and the clarity of the idea of extracting beam sizes from radiation characteristics, this scheme has side effects that can lead to incorrect interpretation of the results. For example, the interaction between target elements can lead to the appearance of resonances in angular distributions, even if the particles are located at large distances from each other [48].

However, using the obtained expressions, one can choose the target parameters (particle size, period) in such a way that at the considered frequency these resonances will not be noticeable comparing with the diffraction maxima.

The spectral-angular distribution of the radiated energy at far distances is described by the following formula:

$$\frac{d^2W(\mathbf{n}, \omega)}{d\omega d\Omega} = |\alpha(\omega)|^2 \frac{e^2 \omega^2 c}{\pi^2 v^4 \gamma^2} \left| \sum_e e^{-i\omega \frac{x_e}{v}} \sum_{m_x=-N_x}^{N_x} \sum_{m_y=-N_y}^{N_y} e^{id_x m_x \varphi_x} \left[\mathbf{k}, \left[\mathbf{k}, \mathbf{P}(|\boldsymbol{\rho}_m - \boldsymbol{\rho}_e|) \right] \right] \right|^2. \quad (20)$$

Here e is the electron charge, $\alpha(\omega)$ the polarizability of the particles, which describes how the particle reacts on the external field, ω the frequency of the radiation, v the speed of electrons, c is the speed of light in vacuum, $2N_{x,y} + 1$ defines the number of particles in corresponding direction, \mathbf{k} is the wave-vector of the radiation, $d_{x,y}$ are the periods of the target,

$$\boldsymbol{\rho}_m = \mathbf{R}_m - \mathbf{v}(\mathbf{v}, \mathbf{R}_m)/v^2, \quad (21)$$

$$\boldsymbol{\rho}_e = \mathbf{r}_e - \mathbf{v}(\mathbf{v}, \mathbf{r}_e)/v^2, \quad (22)$$

\mathbf{r}_e is the radius-vector of the electron in a beam and the sum in equation (20) is over all electrons in a beam, \mathbf{R}_m – is the radius-vector of the m -th particle of the target and the other sum in equation (20) is over all particles in the target, for the target shown in fig.1(right) we can write:



$$\mathbf{R}_m = d_x m_x \mathbf{e}_x + d_y m_y \mathbf{e}_y, \quad (23)$$

where m_x and m_y are integers,

$$\varphi_x = \frac{\omega}{c} \left(\frac{1}{\beta} - n_x \right), \quad (24)$$

$\beta = v/c$, and n_x is the component of the unit wave vector $\mathbf{n} = \mathbf{k}/k$,

$$\mathbf{P}(|\boldsymbol{\rho}_m - \boldsymbol{\rho}_e|) = \frac{\mathbf{v}}{v} \frac{i}{\gamma} K_0 \left(\frac{\omega}{v\gamma} |\boldsymbol{\rho}_m - \boldsymbol{\rho}_e| \right) - \frac{\boldsymbol{\rho}_m - \boldsymbol{\rho}_e}{|\boldsymbol{\rho}_m - \boldsymbol{\rho}_e|} K_1 \left(\frac{\omega}{v\gamma} |\boldsymbol{\rho}_m - \boldsymbol{\rho}_e| \right), \quad (25)$$

K_0, K_1 are the modified Bessel functions of the zeroth and first orders.

Since the coordinates of all electrons in a beam are unknown, it is necessary to average expression (7) over all \mathbf{r}_e with the function $f(\mathbf{r}_e)$, which determines how the electrons are distributed in the beam. Further, from a practical point of view, it is interesting to consider only coherent radiation, which N_e times more intense, than the coherent one, with N_e being the population of electrons in the bunch. The intensity of coherent radiation is then determined by the formula:

$$\begin{aligned} \left\langle \frac{d^2 W_{coh}(\mathbf{n}, \omega)}{d\omega d\Omega} \right\rangle &= |\alpha(\omega)|^2 \frac{e^2 \omega^2 c}{\pi^2 v^4 \gamma^2} \frac{\sin^2(d_x (2N_y + 1) \varphi_x / 2)}{\sin^2(d_x \varphi_x / 2)} N_e (N_e - 1) \times \\ &\times \left[\sum_{m_y = -N_y}^{N_y} \left[\mathbf{k}, \left[\mathbf{k}, \int d^3 r_e f(\mathbf{r}_e) e^{-i\omega \frac{x_e}{v}} \mathbf{P}(|\boldsymbol{\rho}_m - \boldsymbol{\rho}_e|) \right] \right] \right]^2. \end{aligned} \quad (26)$$

For a Gaussian distribution of electrons, expression (13) takes the form:

$$\left\langle \frac{d^2 W_{coh}(\mathbf{n}, \omega)}{d\omega d\Omega} \right\rangle = |\alpha(\omega)|^2 \frac{e^2 \omega^2 c}{\pi^2 v^4 \gamma^2} S N_e (N_e - 1) \left[\sum_{m_y = -N_y}^{N_y} \left[\mathbf{k}, \left[\mathbf{k}, \frac{\mathbf{v}}{v} \frac{i}{\gamma} \mathbf{A} - \mathbf{B} \right] \right] \right]^2, \quad (27)$$

Where the notation is introduced:

$$\mathbf{A} = \frac{1}{\pi \sigma_y \sigma_z} e^{-\frac{\sigma_x^2 \omega^2}{4v^2}} \int_{-\infty}^{+\infty} dy_e \int_{-\infty}^{+\infty} dz_e e^{-\frac{y_e^2}{\sigma_y^2}} e^{-\frac{(z_e - h)^2}{\sigma_z^2}} K_0 \left(\frac{\omega}{v\gamma} |\boldsymbol{\rho}_m - \boldsymbol{\rho}_e| \right), \quad (28)$$

$$\mathbf{B} = \frac{1}{\pi \sigma_y \sigma_z} e^{-\frac{\sigma_x^2 \omega^2}{4v^2}} \int_{-\infty}^{+\infty} dy_e \int_{-\infty}^{+\infty} dz_e e^{-\frac{y_e^2}{\sigma_y^2}} e^{-\frac{(z_e - h)^2}{\sigma_z^2}} \frac{\boldsymbol{\rho}_m - \boldsymbol{\rho}_e}{|\boldsymbol{\rho}_m - \boldsymbol{\rho}_e|} K_1 \left(\frac{\omega}{v\gamma} |\boldsymbol{\rho}_m - \boldsymbol{\rho}_e| \right). \quad (29)$$

$\boldsymbol{\rho}_m - \boldsymbol{\rho}_e = (d_y m_y - y_e) \mathbf{e}_y - z_e \mathbf{e}_z$. Here $\sigma_{y,z}$ are the transverse sizes of the beam. The integrals in expressions (28)-(29) must be calculated numerically. Thus, expressions (27)-(29) describe the characteristics of the Smith-Purcell radiation excited by an electron beam from a target that is asymmetric in two perpendicular directions. These expressions contain the transverse sizes of the beam, which can be determined experimentally.



Investigation of the influence of the beam emittance on the radiation characteristics in the CST software package.

Methods for Cherenkov diffraction radiation (CDR) application for charged particle beam diagnostic are actively developed today. CDR is an analogue of a diffraction radiation and occurs in a target when the beam passes near its surface. Cherenkov radiation (CR) was discovered in 1934 [49] and was theoretically described by Tamm and Frank in 1937 [50, 51]. Then this radiation generation mechanism began to be widely used in high-energy physics. Today, CR is used to detect and identify various types of charged particles in space physics [52], as well as at accelerators and colliders [53, 54]. It follows from the theory [50] that the intensity of CR depends on the path length of a particle in a substance. Such a dependence makes it possible to obtain large fluxes of radiation photons when using extended media, or in other words - longer emitters. Another feature of Cherenkov radiation is the specific angle - the Cherenkov angle, under which photons propagate ($\cos \vartheta = 1 / \beta n$). The angle depends on the velocity of the particle, determined by β , and to a greater extent on the target material, determined by the refractive index n . From an experimental point of view, it is very important that the Cherenkov angle is large enough with respect to the beam trajectory, so CR is quite easy to distinguish from radiation arising due to other mechanisms, for example, transition radiation (TR), which is produced when a charged particle crosses the interface between two media. Note, CR is a very fast process that allows the construction of detectors with high temporal resolution, limited only by the speed of the readout electronics. Indeed, photons produced by this mechanism are emitted without a time delay, which is typical, for example, for scintillators. This feature of CDR makes it possible to effectively measure the transverse dimensions and profile of the charged particle beam.

The passage of the beam through a substance during measurements leads to its destruction or a significant deterioration in the parameters, which is undesirable at modern facilities, especially at ring accelerators. For this reason, new methods of non-destructive diagnostics are being actively developed and existing ones are being improved. When the beam passes over the target at a certain distance, called the impact parameter, CDR is generated. The CDR intensity in such a geometry is strongly affected by the value of the impact parameter, with an increase of which the radiation intensity decreases. When generating Cherenkov radiation by a particle beam, one can operate both in coherent and incoherent modes.

The coherent mode is achieved when operating at wavelengths exceeding the length (and transverse dimensions) of the beam, and gives an increase in intensity in proportion to the square of the number of particles in it. In the incoherent mode, a linear dependence of the radiation yield on the beam current is observed. When CDR is generated in the coherent mode, it becomes possible to measure both transverse dimensions of the beam [42], due to which it becomes possible to measure the beam divergence - an increase or decrease of its physical volume. Such measurements should eventually make it possible to calculate the emittance as well.

Usually, when calculating the generation of diffraction and Cherenkov diffraction radiation, the particle beam is considered to be non-divergence. This part of the report aims at evaluating of the



effect of beam divergence on Cherenkov diffraction radiation.

At present, in the field of high-energy physics and accelerator physics, computer simulation has become an integral part of any physical experiment as a consequence of detector complexity increasing and high demands on the modern facility accuracy. To simulate the processes of the generation of CR, TR, DR, and CDR, the CST Studio software package [55], namely its module that allows working with charged particles - Particle Studio, is used. The module contains several solvers, two of which: Particle-in-Cell and Wakefield, were used to conduct these studies.

The Particle-in-Cell (PIC) solver determines particles within some physical region defined by the computational mesh. The idea of the method is to find scalar potentials or fields in the entire physical domain using standard grid-based methods such as the Finite Integration Method (FIT), with appropriate initial and boundary conditions, and to interpolate the effective field strength on all particles that are inside the corresponding cell. Once the force acting on each particle is known, we can solve the equations of charged particle motion to obtain new coordinates and velocities. The charge that each particle carries is then reassigned to the nodes of the cell in which it resides, and the above procedure is repeated at each time step until the final simulation time is reached.

The Wakefield solver calculates the fields around the particle beam and the wakefields resulting from interactions with inhomogeneities in the surrounding structure. The particle beam is set as linear one with a Gaussian distribution, Figure 29 shows the distribution of the electric field modulus of such a beam. The PIC solver allows us to specify several different types of primary particle generators, and here a beam emitted from a circular area with a constant cross section and a Gaussian distribution in the longitudinal direction is used. An important fact that it is possible to directly measure the emittance of the diverging beam and its effect on radiation in this solver. However, the field of such a beam (see Figure 30) differs in structure from a beam with a Gaussian longitudinal distribution, so before finding out the reasons for this difference, it was decided to use the Wakefield solver with its generator of linearly moving beams. Since field oscillations in the wake of the beam moving in vacuum critically affect the resulting radiation when such a beam passes over a target.



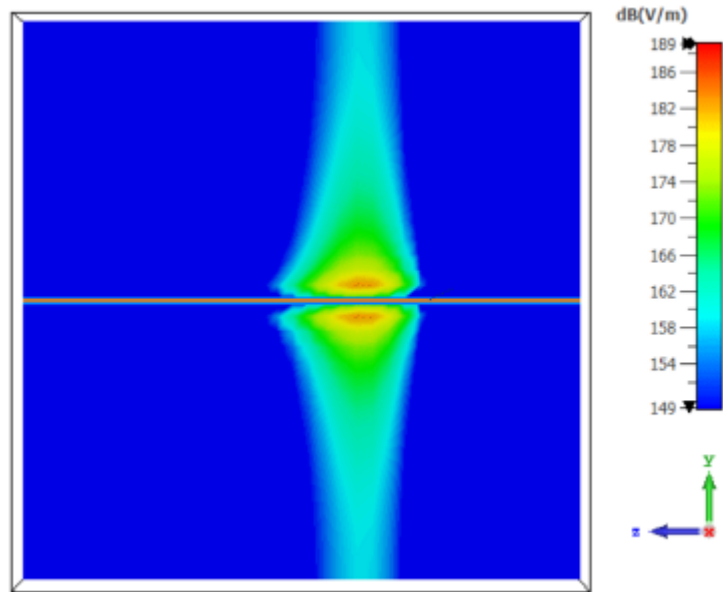


Figure 29. Two-dimensional distribution of the absolute value of the electron beam electric field in the Wakefield solver. A beam of electrons with an energy of 3 GeV. The time is fixed.

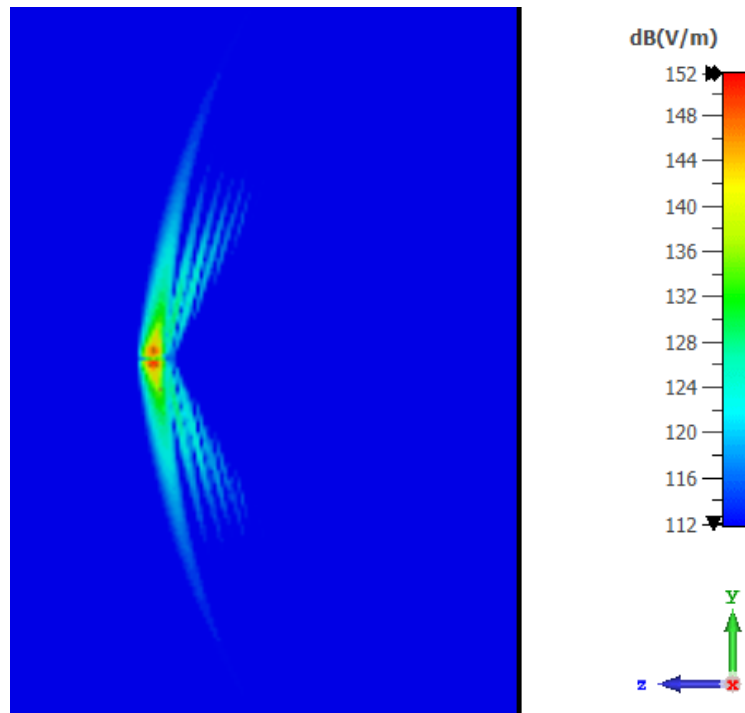


Figure 30. Two-dimensional distribution of the absolute value of the electron beam electric field in the PIC solver. A beam of electrons with an energy of 3 GeV. The time is fixed.

Various targets can be used to generate DR and CDR by an electron beam. In this work, a triangular prism is used - a target shape that has proven itself well in experiments [56] (see the photograph of the target in Figure 31). The triangular shape allows the CDR to leave the target with virtually no refraction. In the simulations, quartz with a dielectric permittivity of 3.75 was used as the target material. A target with a 1 cm edges was placed under a 3 GeV electron beam at a distance of

1 mm (see Figure 31 and 32). The length and transverse dimensions of the beam are 0.2 mm. To take into account the effect of divergence, measurements were carried out for various beam sizes at a fixed number of electrons in it, imitating the situation when a diverging beam flies over successively installed identical targets.

Before carrying out simulations, it is worth making some theoretical estimates of the influence of the beam divergence on radiation with a help of a form factor describing a beam of N particles with a Gaussian distribution [42], since this form factor allows one to move from a one-particle calculations of radiation to a calculation with the beam of electrons, and also contains information about the size of the beam. The form factor can be written as

$$F = NF_{inc} + N(N-1)F_{coh}, \quad (30)$$

where the incoherent and coherent parts can be described as

$$F_{inc} = \frac{1 - \Phi(\sigma_z \rho - h/\sigma_z)}{1 + \Phi(h/\sigma_z)} e^{\sigma_z^2 \rho^2}, \quad (31)$$

$$F_{coh} = \frac{\left(1 - \Phi\left(\frac{\sigma_z \rho - h/\sigma_z}{2}\right)\right)^2}{\left(1 + \Phi(h/\sigma_z)\right)^2} e^{\frac{\omega^2 \sigma_x^2}{2c^2 \beta^2}} e^{\frac{k_y^2 \sigma_y^2}{2}} e^{\frac{\sigma_z^2 \rho^2}{2}}, \quad (32)$$

where Φ is the error function, $\rho = \frac{\omega}{\gamma \beta c} \sqrt{1 + \gamma^2 \beta^2 n_y^2}$, $\beta = v/c$ – is the dimensionless velocity of a charged particle emitting radiation at frequency ω , c is the speed of light, $\gamma = 1/\sqrt{1 - \beta^2}$ is the Lorentz factor, \mathbf{k} is the wave vector, $\mathbf{n} = \mathbf{k}/k$ is the unit vector in the direction of the wave vector, h is the impact factor, and $\sigma_x, \sigma_y, \sigma_z$ is the dimensions (half) of the beam in the longitudinal and transverse directions, respectively. Here the coordinate system is chosen such that the bunch moves along the x axis and the z axis is perpendicular to the target surface. It is convenient to specify the unit vector of radiation observation as $\mathbf{n} = (\cos \theta, \sin \theta \cos \varphi, \sin \theta \sin \varphi)$. Note, in the theory, beam divergence is understood as an increase in the real size of the beam while maintaining its charge, which can lead to different results when compared with simulation, which also takes into account the divergence in the phase space.

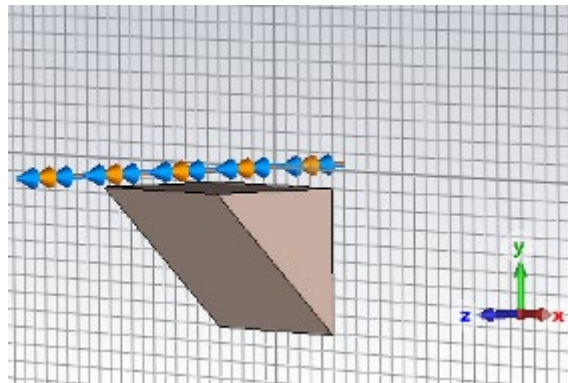
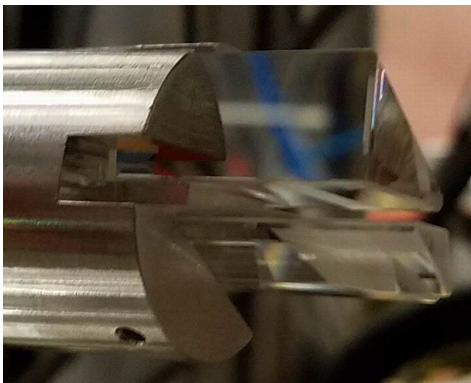


Figure 31. Left: Photograph of targets in holder [56]. Right: Target placed under the particle beam in the CST program.

Figure 33 shows the dependence of the expressions for the incoherent (31) and coherent (32) form factors on the beam sizes, while maintaining the number of particles in it, at a fixed wavelength of 300 μm and for an observation angle equal to the Cherenkov angle in quartz for 3 GeV electrons (58 degrees). It can be seen that for the selected parameters, the incoherent form factor is equal to unity and does not change with the size, while the coherent factor quickly decreases and goes to zero at beam half-widths equal to half of the wavelength.

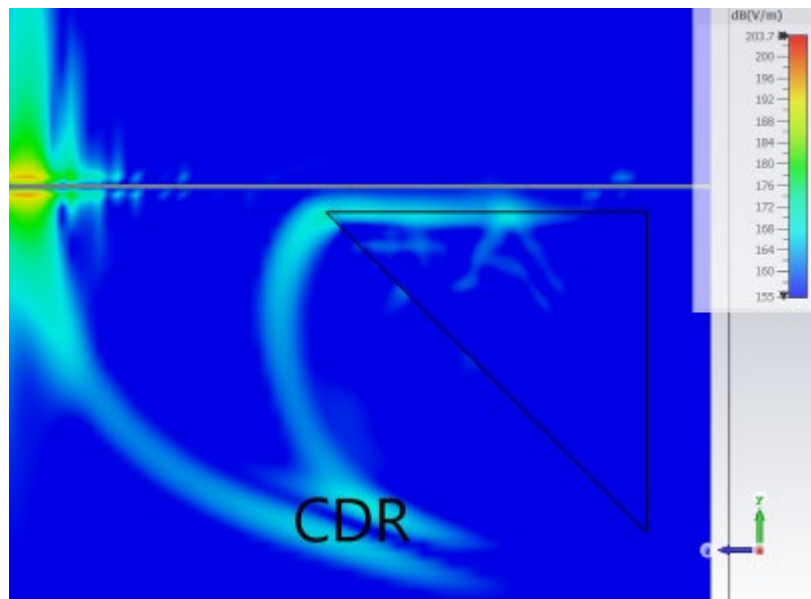


Figure 32. Two-dimensional distribution of the absolute value of the electric field of the electron beam and radiation initiated by it in the Wakefield solver. The time is fixed.

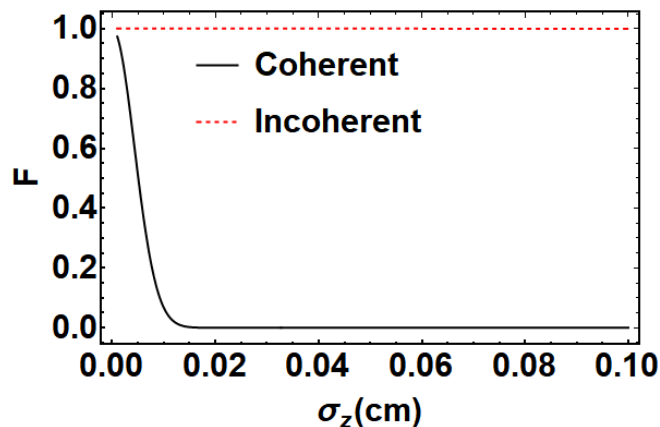


Figure 33. Dependence of the coherent (black) and incoherent (red) form factors on the beam size, while maintaining the number of particles in the beam, the radiation emission angle is equal to the Cherenkov angle in quartz for 3 GeV electrons (58 degrees), the impact parameter is 1 mm.

Now let us move to the simulation results in CST Particle Studio. Figure 32 shows the two-dimensional distribution of the absolute value of the electric field strength at a fixed point in time -

after the electron beam interacted with the target. At the bottom of the figure, one can clearly see the CDR that has emitted from the target and has almost completely separated from the beam field. The radiation generation is even more clearly visible in Figure 34, which shows the two-dimensional distribution of the absolute value of the electric field for the entire observation time (integrated over time) at a fixed phase. This figure shows that the radiation is refracted at a small angle (shown by arrows), which allows it to leave target with the least loss for further registration. To use this method in the experiment, the angle of the triangular prism must be chosen properly to avoid even such refraction.

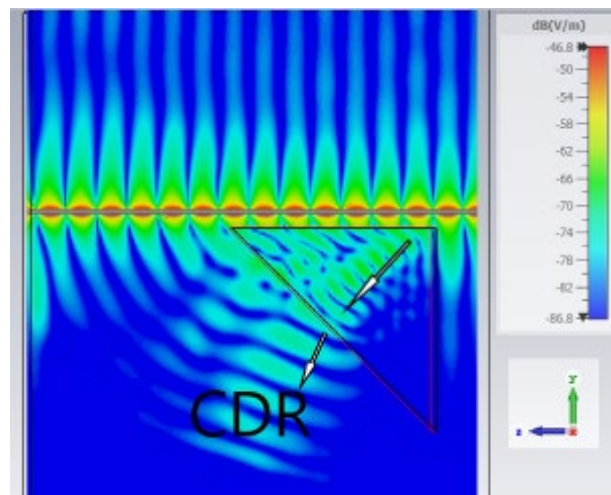


Figure 34. Two-dimensional distribution of the absolute value of the electron beam electric field and radiation initiated by it with fixed phase integrated over the observation time. Phase is 90 degrees, frequency is 1 THz. The arrows show the propagation direction before and after refraction at the prism boundary.

To estimate the effect of the beam divergence on the radiation, several simulations were performed for σ_x , σ_y , σ_z varying from 0.025 mm to 0.5 mm, with a constant impact parameter of 1 mm, an electron beam charge of 1 nC, and a fixed frequency of 1 THz. Measurements at a frequency of 1 THz were carried out using the PowerFlow field monitor (see Figure 35), and further integration the radiation power over the volume of the counting space.

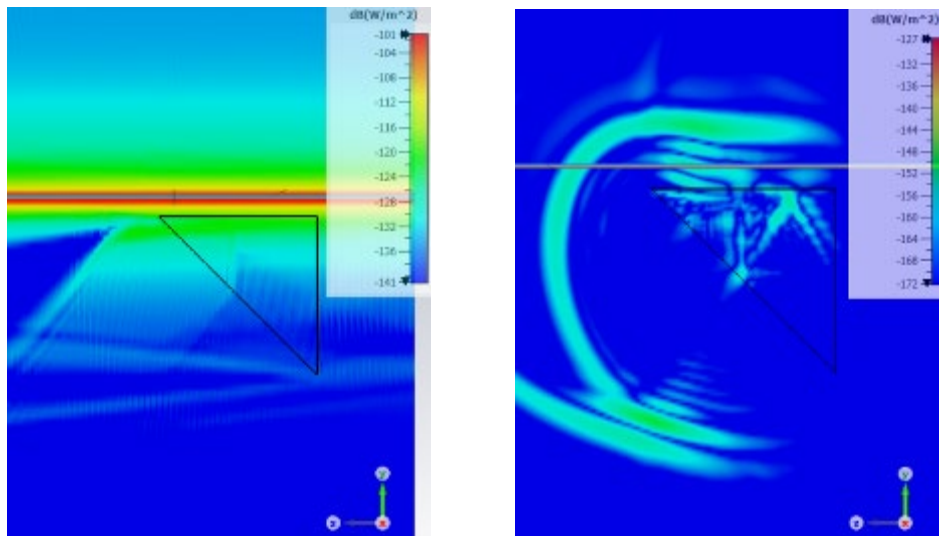


Figure 35. Two-dimensional distribution of the absolute value of the electron beam electric field and radiation power. The measurement was carried out using a PowerFlow beam monitor with σ_x , σ_y , σ_z equal to 0.05 mm (left) and 0.3 mm (right).

Measurements using integration over the volume lying below the plane of the upper face of the prism showed that, as the theory predicted, with increasing dimensions, the radiation power at the selected frequency drops sharply between 0.05 mm and 0.15 mm, then the decrease becomes more gradual. The reason for this behavior is the termination of operation in a coherent mode with respect to the measured frequency. In the case of a large divergence and a complete loss of coherence, the measurement of dimensions using this method will require an increase in the measured radiation wavelength.

Conclusion

Determining the emittance of an electron beam in a synchrotron ring storage ring is a well-established procedure, which for synchrotrons is based on the use of the synchrotron radiation itself and the beta function of a particular machine. The interference scheme based on measuring the interferogram from a double-slit target with subsequent reconstruction of the transverse beam size and calculation of the emittance from the known beta function gives the highest accuracy at the moment. Ultralow emittances and a sharp asymmetry of the beam cross section, which are typical for synchrotrons of the 4th generation, require a significant improvement in existing methods or the development of new ones. At this stage, we have developed a physical and mathematical description of a promising scheme for nonperturbing diagnostics of ultrarelativistic electron beams with strongly asymmetric cross sections, based on the use of the Smith-Purcell effect from a target, which is a two-dimensional photonic crystal. Also, we performed computer simulation of another promising diagnostic mechanism based on Cherenkov diffraction radiation in the CST software package. It is shown that an increase in the beam size due to its divergence leads to a decrease in the radiation intensity during the transition from coherent to incoherent generation.

6.3 Purity Monitor

Bunch Purity measurements is a measurements of a bunch longitudinal distribution with a high dynamic range. The bunch purity, defined as the ratio of the counts for the peaks caused by the impurity bunches to those for the peak caused by the main bunch, is needed to be kept sufficiently low not to interfere with the time structure produced by the beam from the main bunch [57].

Measurement of the special fill patterns of synchrotron light sources is important for time-resolved experiments, looking at very weak decay signals as seen in Mossbauer spectroscopy. For that experiments the adjacent buckets should contain as few as possible of any stored particles. The main mechanisms of filling neighbor buckets are [58]:

- Quantum lifetime. An electron is lost from a bucket by emitting a photon having a momentum larger than bucket height and can be re-captured in a neighboring bucket.
- Lifetime determined by the vacuum pressure. Electrons lose energy in collisions with residual gas molecules in the vacuum chamber and can be re-captured in a neighboring bucket.
- Touschek effect. Electrons in a bunch execute betatron oscillation with transverse momenta. When two electrons are scattered elastically, the transverse momenta can be transferred to the longitudinal plane. The electrons can be re-captured by the forward or backward bucket, respectively.
- Injection errors (energy, timing). Incorrect timing and energy matching at injection can cause a growth on the both sides of the main buckets. This becomes even more important at topping up injections.

A method with very good time resolution ($\ll 1$ ns for RF frequency 352.2 MHz and bunch length ~ 10 ps) and high dynamic range (more than six orders of magnitude) is necessary to sufficiently measure the contents of the neighbor buckets relative to the main bucket. The longitudinal profile of the selected bunch in the beam filling pattern within the storage ring should be measured, with several RF buckets around it.

Measuring method

To measure the longitudinal profile of the electron beam in a light source with good time resolution and high dynamic range, synchrotron radiation of the electron beam after a bending magnet is used.

A typical setup to measure the bunch purity is a time-correlated single photon counting method – TCSPC. The TCSPC is based on the fact that the number of photons produced when the beam is passing through a bending magnet is directly proportional to the number of electrons in the beam. Therefore, the fill pattern can be obtained by measuring the temporal distribution of the synchrotron radiation, which corresponds to the distribution of the electron beam. In that method, to build the longitudinal bunch distribution, the arrival time of individual photons relative to a clock pulse which is synchronized to the bunch revolution frequency via the storage ring RF system, is measured, integrated over a very high count ($\sim 10^9$), or over several minutes. In that case, synchrotron radiation from bending magnet should be registered by some type of photodetectors,



and that detector should produce single pulses to pulse time measuring system with the probability of generating a single pulse is much less than one per beam revolution.

Detector selection.

The choice of the structure of the measurement system is largely determined by the selected synchrotron radiation detector.

Measurements of the bunch purity have often been tried by detecting visible light with a photomultiplier tube (PMT) [59], or by detecting X-rays with a plastic scintillation detector and PMT [60]. However, these methods have suffered from a relatively high background caused by the detector itself or by stray light. Thus, the measurable purity was at most 10^{-5} . Additionally, time resolution of the scintillation detectors is poorer than 1.3 ns at 14.4 keV. They also have some problems of noise pulses mainly from a photomultiplier tube (PMT) or a slow component of scintillation light, which worsens the peak-to-background ratio.

In contrast, the APD detector has a good time resolution of 100 ps (FWHM), a short tail on the peak profile, and very low noise level. An APD is a diode doped so that when reverse bias is applied there is a region of high electric field ($\geq 10^5$ V/cm) which causes charge carriers entering that region to undergo gain due to impact ionization. The APD detector detects X-rays directly without a scintillator and is operated in linear mode to obtain a fast pulse for good timing performance.

The APD Hamamatsu S12053-10 [61] (early this name was S5343) is selected. The device is a silicon planar epitaxial reach-through APD, and has a structure consisting of an epitaxial π (low concentration of p^- impurity) depletion layer 10 μm thick on an n^+ wafer 500 μm thick and a p^+ layer less than 1 μm thick, fabricated on the top of the π layer. The side of the p^+ layer is irradiated by an X-ray beam and the detection area is 0.8 mm^2 (1 mm in diameter). A high electric field of more than $2 \cdot 10^4$ V/cm is applied to the depletion region in the reach through type. This APD is designed in such a way that the π layer is fully depleted except the p^+ layer when a sufficiently high reverse bias-voltage is applied. When an X-ray arrives at the depletion region, photoelectrons caused by the photoelectric effect generate electron-hole pairs. The carriers are collected at each electrode in the high electric field of the drift region. The electron carriers are multiplied in a p-n (n^+) junction and the APD has an internal gain of $10^2 - 10^3$. Let's consider more important characteristics of that APD [57]:

- 1) *Time resolution.* The reason why the APD detector had a sub-nanosecond resolution is first that the detector does not use a scintillator. The timing of the outputs does not depend on the decay of scintillation lights in which the decay constants are 1-2 ns for plastic scintillators since X-rays are directly absorbed by silicon in the APD detector. Though the APD detector has a fluctuation caused by the difference of the transit times for collecting the electrons from where they are generated by an incident photon, the transit times themselves are very short, of the order of hundred picoseconds.

The timing uncertainty in the APD depends mainly on a finite time that the electron



carriers require to transit the depletion layer from the point generated by an X-ray; the available timing naturally distributes from a value obtained by the electrons generated near the n + region, to that obtained by the electrons generated at the far side of the depletion layer near the p + region. Since the drift velocity of the electron carriers has a saturation value of approximately 10^7 cm/s at 300 K for an electric field of more than $2 \cdot 10^4$ V/cm [62] and the present device is designed to obtain this saturation value in the depletion region, the 100 ps resolution of the detector is therefore reasonable for a depletion layer of 9 μ m.

- 2) *Dynamic range.* The use of an APD removed the random noises which are caused by thermal electrons emitted from the PMT's cathode or by natural radioactive isotopes contained in a scintillator and a PMT glass. Since electronic noises could be perfectly discriminated from the signals by the difference of their amplitudes, the APD detector had a peak-to-background ratio of larger than 10^7 with simple electronics.

The APD device is made of highly purified silicon to a small impurity concentration. Thus, natural radioactivity contained in detector materials is negligible though radioactive elements such as ^{40}K often contribute to the background in the methods using a PMT.

With a surface area about 1 mm^2 and a thin detecting depth about 10 μ m, the detecting volume of an APD device is very small. Thus, cosmic rays are hardly caught by the device and can hardly contribute to develop background pulses.

The residual background is due primarily to electric sources, such as leakage current from an APD device. However, the noises can readily be removed with adjusting a discrimination level of pulse amplitude because the APD is operated in linear mode and in which the signal-to-noise ratio on amplitude is more than 4.

- 3) *Detection efficiency.* The efficiency depends on the thickness of the depletion layer of silicon APD. Although the time resolution becomes better with a thinner depletion layer, a device having a detection depth much thinner than 10 μ m will not have sufficient efficiency for detecting X-rays. After all, the value of 100 ps may be regarded as an ultimate resolution of the APD detector practically useful for X-ray region.

Measurement system structure

The structure of the measurement system is determined both by the requirement for the pulse rate after the detector, with the probability of generating a single pulse is much less than one per beam revolution; and by the need to reduce the radiation dose at the detector. Additionally, the energy of the X-ray photons recorded by the APD must be limited to increase the fraction of recorded photons [63]. To meet these requirements, the APD must record secondary scattered X-rays from a metal absorber fired by hard X-ray synchrotron radiation in a beamline after the bending magnet.

The detecting system of the purity monitor, as it was developed for the ESRF light source [64], is shown on Figure 36. An avalanche photodiode collects scattered x-ray photons from a copper x-ray absorber on an unused bending magnet beamline. When copper is bombarded with hard x-rays



some electrons transitions to the innermost K shell from a 2p orbital of the second, or L shell are excited, and soft x-rays (about 8 keV) are emitted [65]. The so called $K\alpha$ and $K\beta$ transitions are very fast (order of 10 ps) so they can be used to detect indirectly the arrival time of the photons. The fluorescence yield is around 50% for copper. This means that roughly half of the x-rays that are absorbed will produce the transition and generate softer x-rays, while the others will generate Augers electrons.

An aluminum window will transmit a moderate flux of Compton scattered photons from the Cu absorber surface within vacuum chamber to APD, placed near the chamber. These photons will be heavily attenuated by the aluminum window. The avalanche photodiode must be protected within a thick lead housing to prevent erroneous counting from x-rays scattered from other sources than the Cu absorber surface (that would not have the correct timing) as well as Bremstrahlung gamma rays coming directly from the electron beam impacting residual gas atoms in the storage ring. A cap and a glass window attached to an APD were removed to allow X-rays to reach directly the surface of the APD.

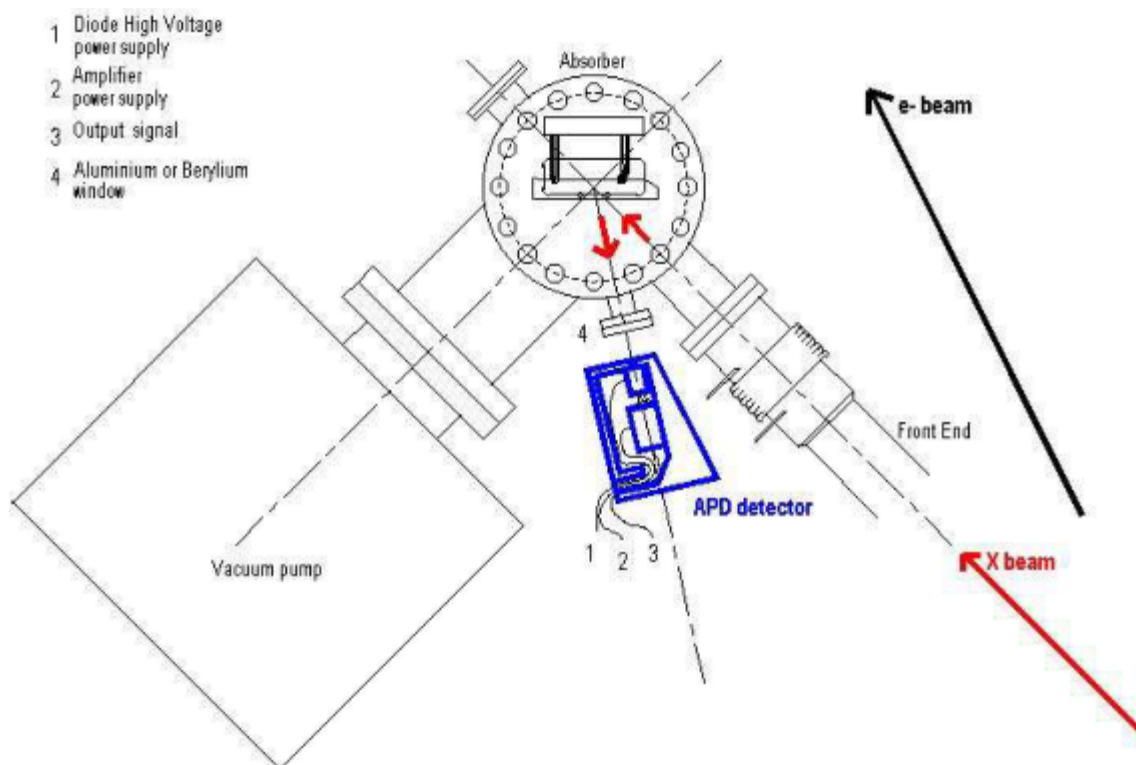


Figure 36. Purity Monitor detector system.

The APD detector consists of a silicon reach-through APD and a simple circuit of a resistor and a capacitance for stably applying the reverse bias voltage. The APD detector is operated in linear mode to obtain a fast pulse for good timing performance. The detector was operated at room temperature and at the applied voltage of 150 V, which was 3 V below the breakdown voltage. The internal gain of the APD was estimated to be about 60 from measurements of charge quantity per pulse with a charge-sensitive preamplifier instead of the fast amplifier. Current pulses from the detector should be amplified and converted to voltage pulses with a fast amplifier with a gain of

order 10^2 and bandwidth of several GHz, to maintain a fast response of the APD device.

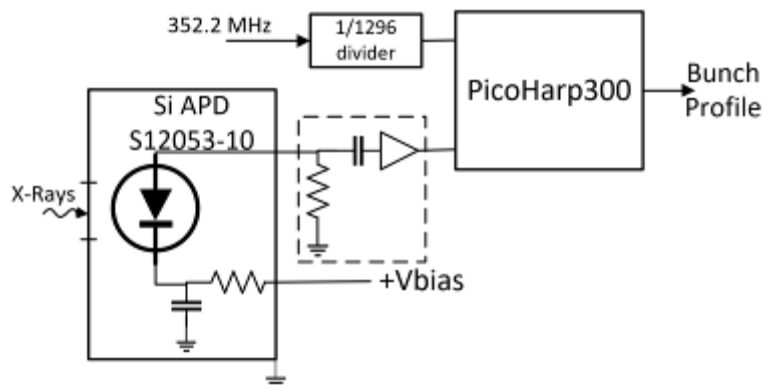


Figure 37. Purity Monitor System.

Digital measurement unit – TDC

Previously, the time difference between single pulses from the APD module and a clock pulse synchronized to the bunch revolution frequency with ps resolution should be measured with self-made electronic schemes [57, 66]. These schemes should include: RF frequency divider for rf clock from a storage ring timing system; clock pulse delay unit; a constant-fraction discriminator (CFD) for pulses from the APD module; a time-to-amplitude converter (TAC), which measure time difference between two clock signals; a fast analog-to-digital converter, which digitizes the TAC's outputs with a high rate; a multichannel analyzer, which is used to record time spectra of the bunch structure.

Now much part of that functionality is realized within PicoHarp300 device from PicoQuant [67].



Figure 38. Stand Alone TCSPC Module - PicoHarp 300.

PicoHarp300 measures the time difference between two pulses and build a histogram of the

pulses. It requires two pulses of negative polarity, 0.5 to 30 ns in duration, with a rising edge of less than 2 ns and a desired amplitude of 200 to 400 mV. It contains pulse delay unit with 100 ns range and 4 ps step. The block diagram of the device is shown in the Figure 39.

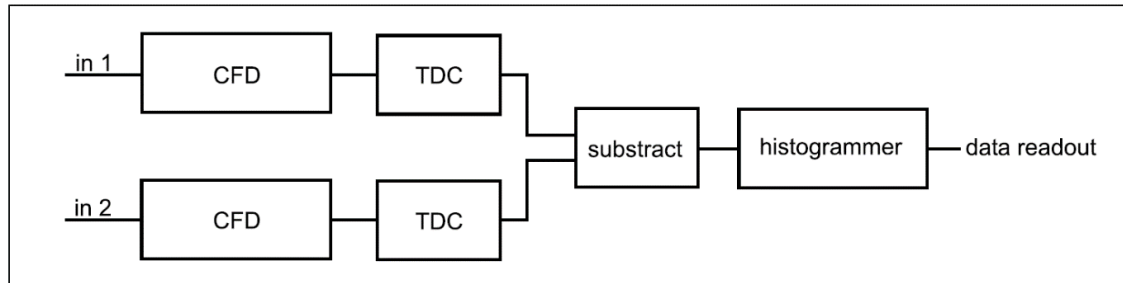


Figure 39. Block diagram of a modern TDC based TCSPC system running in classical histogramming mode.

The Constant Fraction Discriminator (CFD) is used to extract precise timing information from the electrical detector pulses that may vary in amplitude. The CFD is very important as their pulse amplitudes vary significantly. The most common way of implementing a CFD is the comparison of the original detector signal with an amplified and delayed version of itself. The signal derived from this comparison changes its polarity exactly when a constant fraction of the detector pulse height is reached. The zero-crossing point of this signal is therefore suitable to derive a timing signal independent from the amplitude of the input pulse. Modern CFDs basically detect the vertex of each pulse and trigger on that point, which is easier for implementation. In addition, typical CFDs allow a so-called discriminator level to be set, which defines the lower limit that the detector pulse amplitude must pass. Random background noise pulses can thereby be suppressed.

In the classical design the signals from the CFD and SYNC trigger are fed to a Time to Amplitude Converter (TAC). This circuit is essentially a highly linear ramp generator that is started by one signal and stopped by the other. The result is a voltage proportional to the time difference between the two signals. But the ADC, that measures that voltage, must be very fast in order to keep the dead time of the system short, must guarantee a very good linearity over the full range, which is difficult for high resolution, from 12-bit ADC.

The tasks performed by TAC and ADC can be carried out by a single fully digital circuit, a so-called Time to Digital Converter (TDC). These circuits can measure time differences based on the delay times of signals in semiconductor logic gates or the conductor strips between them. The relative delay times in different gate chains can be used to determine time differences well below the actual gate delay. Other TDC designs use interpolation techniques between the pulses of a coarser clock. This permits exceptionally small, compact and affordable TCSPC solutions, as the circuits can be implemented as Application Specific Integrated Circuits (ASICs) at low cost and high reliability. Modern TCSPC devices have independent TDCs for each input channel. The important detail is that the individual TDCs are running off the same crystal clock. If a timing difference is needed, it can be obtained by simple arithmetic in hardware.

The histogrammer has to increment each histogram memory cell whose digital address in the

histogram memory it receives from the calculated time difference, and sophisticated TCSPC systems switched between two or more memory blocks, so that one is always available for incoming data.

When measuring, you need to vary the intensity (the number of X-ray photons) on the APD and watch how the pulse shape changes on the histogram – if the pulse becomes shorter with increasing intensity, this indicates that there are too many photons between two pulses from the timing system.

6.4 Bunch Length Measurements

Longitudinal profile with ps time resolution is measured with the streak camera for synchrotron radiation from the bending magnet in visible light range.

Mirror Chamber

The synchrotron radiation will come from the entrance of the first longitudinal gradient bending magnet (DL1A_5), where the magnetic field is 0.45T. Synchrotron radiation should be reflected to the visible light detector system by the mirror, installed within the vacuum chamber on the beamline [5]. Light Mirror Vacuum chamber is shown on Figure 40.

An in-vacuum mirror will extract the light to the periscope trough a view-port. The mirror will be located inside the vacuum chamber CH4, about 4 m from the synchrotron radiation source, the visible light radiation size on the mirror is about 10 mm on the vertical axis. A light extraction system uses a vertically movable mirror with a thermal probe in a feedback loop in order to avoid mirror surface deformation by the thermal load from the X-ray source. The mirror will select only the upper part of the radiation and its temperature is continuously monitored by two thermocouples. However, the in-vacuum mirror is water cooled and can be inserted and used as a "full-mirror" when operating at very low current for machine studies.



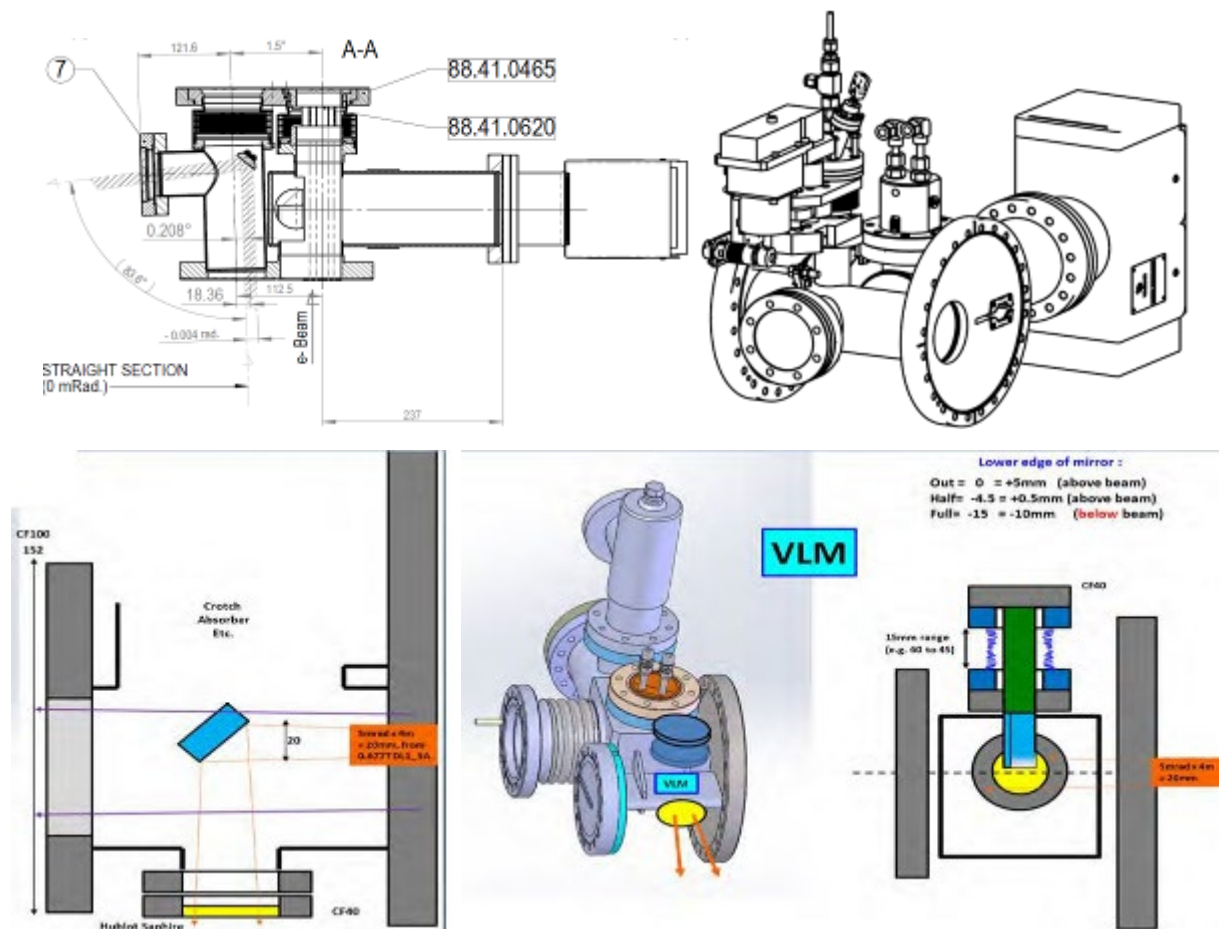


Figure 40. Light Mirror chamber for Bunch Length Monitor.

The main elements of the assembly of the mirror system are:

- mirror movement mechanism: a stepper motor (apparently with a reducer) moves the assembly along two rods with the stepper motor itself, the flanges of the cooling systems and the terminals of the temperature sensors, and a mirror fixed to it through the rod, through the bellows relative to the fixed connector on the vacuum chamber. Stroke depth is 5 mm.
- Mirror water cooling: inside the movable stem, through the bellows, through the water connector assembly on the outer movable flange.
- Thermocouples (2 pcs., for duplication), and wires from them to an external movable connector.

The whole assembly is movable in vacuum by the application of a vacuum chamber with bellows and vertical motorization. A simple software loop will provide the feed-back which controls the vertical position of the mirror in order to keep the temperature of the thermal probe at $\sim 55^{\circ}\text{C}$. In this way the mirror piece itself is kept as close as possible to the heart of the beam without absorbing more than $\sim 1\text{W}$ of beam power. It is $\sim 0.5\text{mm}$ above the heart of the beam which means that $\sim 45\%$ of the available light flux is extracted.

The time response of the loop should be no worse than 100ms, which is sufficient to react to slow, vertical, electron beam orbit drifts or to beam injection. A hardwired Machine Interlock ensures that at temperatures $>70^{\circ}\text{C}$ the electron beam is instantly cut in order to guarantee a fail-safe protection of the mirror in the exceptional case of very unstable beam.

In order to minimize the passage of unwanted radiation, the hole in the storage shielding should be drilled below the electron orbit plane. A periscope system composed of two motorized mirrors has been designed to guide the light through the storage ring tunnel wall to the optical hutch and another mirror will deflect it to the optical table.

Streak Camera

Bunch length measurements will be performed with a 1ps resolution Streak Camera that uses synchroscan streaking at $1/4$ RF and a dual time base enabling measurements on one or several bunches on a turn-by-turn basis.

The streak camera is a device to measure ultra-fast light phenomena and delivers intensity vs. time vs. position (or wavelength) information. These cameras would "streak" reflected light onto film. Figure 41 shows the operating principle of the streak camera [68].

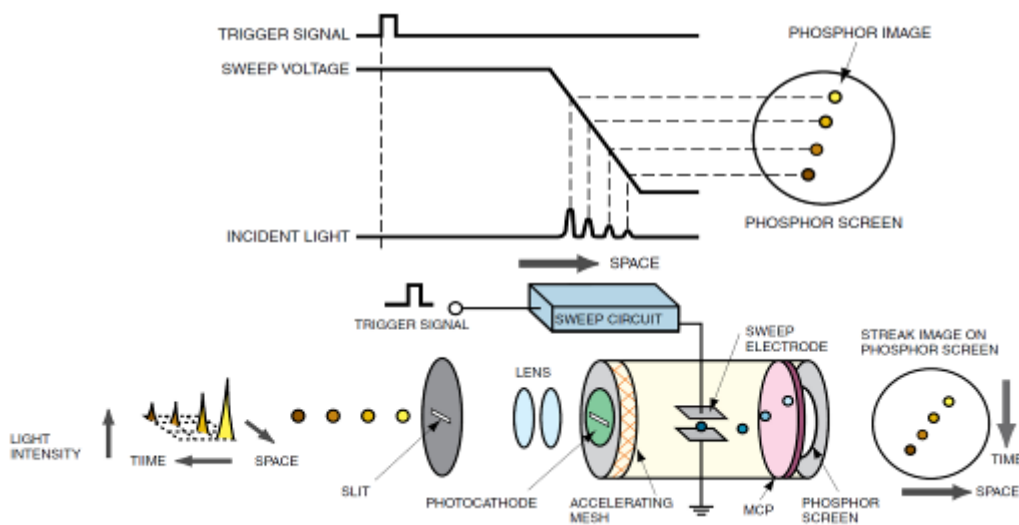


Figure 41. Operating principles of the Streak Tube.

In short, light flux truncated by slit or pinhole, focused by lenses on photocathode that produce electron shower proportional to flux; then it deflected by short front sweep pulse to MCP & Phosphor Screen, and generate timing distribution picture:

- The light being measured passes through a slit and is formed by the optics into a slit image on the photocathode of the streak tube.
- The incident light on the photocathode is converted into a number of electrons proportional to the intensity of the light.
- They then pass through a pair of accelerating electrodes, where they are accelerated and bombarded against a phosphor screen. As the electrons pass between a pair of

sweep electrodes, high voltage is applied to the sweep electrodes at a timing synchronized to the incident light, which initiates a high-speed sweep. During the high-speed sweep, the electrons, which arrive at slightly different times, are deflected in slightly different angles in the vertical direction, and enter the MCP.

- As the electrons pass the MCP, they are multiplied several thousands of times, after which they impact against the phosphor screen, where they are converted again into light. An internal MCP intensifier permits pure single shot measurements at Machine currents below 100mA. This MCP is gateable (50ns) with a few MHz repetition rate and a specially developed programmable gating pulse generator enhances the scope and flexibility of its use. This generator, the dual time base, CCD read-out camera and video digitizer are all synchronized to the orbit frequency so that stable 'life' video images are produced at 8Hz.
- The vertical direction on the phosphor screen serves as the time axis. The brightness of the various phosphor images is proportional to the intensity of the respective incident optical pulses. The position in the horizontal direction of the phosphor image corresponds to the horizontal location of the incident light.

Streak Camera Dual Time Base possibility

By applying a ramp voltage to the additional horizontal deflection plates, the repeated vertical sweep shifts in the horizontal direction (horizontal sweep). This allows temporal information to be captured in the horizontal direction as well as the vertical direction. The vertical axis represents the fast time axis, while the horizontal axis shows the slow time axis. By having two time axis, it is possible to measure pulse widths and phase fluctuations which are sufficiently longer than the repetition frequency of events which repeat at highspeed.

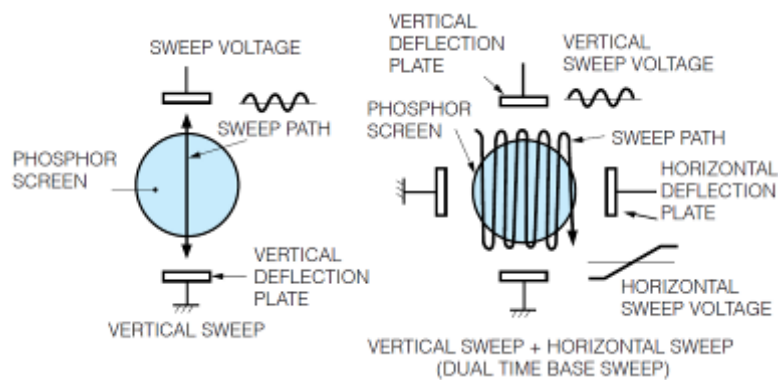


Figure 42. Sweep Path Using Dual Time Base.

The dual sweep axis is a very important extension to a basic streak tube functionality. It requires a second set of deflection plates oriented perpendicular to the plates used for the fast time-space conversion.

Applying a 'slow' HV ramp deflection to these plates equips the streak camera with a dual time axes. In addition to the ultra fast sweep (typically 500ps full scale) there is now a 'slow' (typ. 100ns to 10ms) sweep at right angle. In the two-dimensional output image of the streak camera

(read out by a CCD camera with say, 20ms integration time) these dual times axes are now very conveniently represented as horizontal (slow) and vertical (fast).

This dual time axis allows one to obtain numerous streak images in the same output image if the light input signal and its fast sweeping is repeated. If the slow time scale on the dual axis is well adapted to the repetition frequency, then the individual streaks of consecutive light impulses will be staggered (horizontally) next to each other. This allows the visualization and the measurement of the (slow) time evolution of characteristics of the ultra fast light signal such as duration, profile, and phase stability.

In order to fully benefit from this dual time axis, it is important that the fast sweeping can be repeated at a suitable frequency. For the needed HV deflection signal, that is correctly timed and stable in phase with the repetitive light impulses, two kinds of operation modes exist:

1) Synchroscan operation: The deflection signal is a sinusoidal HV of a high but fixed (pre-tuned) frequency somewhere in the 50-250MHz range. The needed electric trigger signal is in particle accelerators or storage rings

generally obtained from the master source of the RF cavity, at the same frequency or at a sub-harmonic. The attainable phase stability (jitter) is good: 2ps or less. It can even be improved further by internal phase-locked loops, and the trigger signal can be optical (e.g., from a laser oscillator) through the use of special pin-diodes. The range of available sweep speeds and their linearity is somewhat limited but usually more than sufficient.

2) Repetitive Single Shot: Compared with the synchroscan mode the range of sweep speeds is larger and faster, their repetition rate is freely selectable but only up to a few kHz and generally the jitter is worse (>10ps).

Streak Camera Measurement System

The Streak Camera Hamamatsu C10910 [69] has a 200-850nm spectral sensitivity and uses an internal MCP intensifier with a gain range of $3e3$ that is gateable down to 50ns. The fast sweep is continuous at 88.05MHz (i.e., 1/4 RF ESRF) with full time ranges between 80ps and 2ns which offers a temporal resolution down to 1ps.

Using, in addition, a dual time base module (with ranges between 100ns and 100ms) means that several individual bunches in the Storage Ring can be measured on a turn-by-turn basis over many consecutive turns.



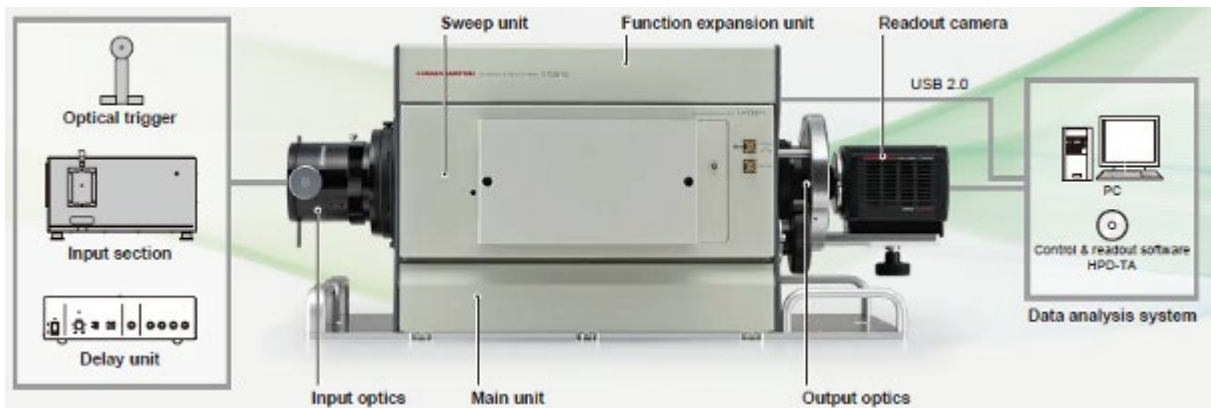


Figure 43. C10910 Universal streak camera system.

The trigger section controls the timing of the streak sweep. This section has to be adjusted so that a streak sweep is initiated when the light being measured arrives at the streak camera. For this purpose, we use a delay unit, which controls how long the trigger signal which initiates the streak sweep is delayed, and a frequency divider, which divides the frequency of the external trigger signal if the repetition frequency of the trigger signal is too high. Also, in cases where the trigger signal cannot be produced from the devices such as a laser, it has to be produced from the light being measured itself, and this requires a PIN photodiode.

The readout section reads and analyzes streak images produced on the phosphor screen, which is on the output side of the streak camera. Because the streak image is faint and disappears in an instant, a high-sensitivity camera should be used. Analysis of streak images is done by transferring the images through a frame grabber board to a computer.

The extracted dipole light is focused by an external achromat through the pinhole of the streak camera. An internal relay lens focusses this light onto the photocathode. The dimensions of the pinhole determine the spatial resolution which, together with the streak speed used, determines the temporal resolution, e.g., a 30 μm pinhole gives a spot size of 7pixels fwhm which results in a time resolution of 7ps with a 500ps streak time scale ($\sim 1\text{ps}/\text{pixel}$). For special Machine Physics other pinholes or the slit aperture were used together with telescope optics that preserve the transverse dimensions of the electron beam. For applications where only the longitudinal dimension (S , time) is of interest the input light beam will be truncated transversely (i.e., pinhole or slit).

Streak Camera Synchronization

The USSR's acceleration frequency (RF) is at 352.2MHz with an orbit frequency at 272Khz (RF/1296). A variety of filling patterns are possible: uniform filling mode 1296 bunches in each RF bucket, ~ 195 mA; 7/8 +1 mode: 1134 grouped bunches + one 4-8 mA bunch; 16 equally distributed over the circumference single bunches, 90mA; 4 equally distributed bunches; a combination of both (Hybrid fill). The consequent light input frequency is either 352.2MHz, 4.35Mhz or 272KHz ($T=2.8\text{ns}$, 230ns or 3.68mks respectively).

The C10910 Streak Camera requires 3 trigger signals: the vertical (fast) streak deflection that provides a permanent sinusoidal deflection with excellent jitter; the horizontal dual time base slow



deflector; the photocathode and MCP intensifier gate. And additional trigger signal to readout digital camera. All trigger signals should be synchronized with 352.2 MHz storage ring master frequency, to obtain stable repeated results. Trigger signals requirement for these units are determined by input characteristics of expansion units, which provide corresponding functionality.

The vertical (fast) streak deflection is provided by synchroscan unit, which can generate a high-speed repeated sweep to the deflection electrodes, which provide <1 ps temporal resolution. This sweep frequency is factory set within 74 MHz to 165 MHz range, with one of 5 selectable sweep time, from 80 ps to 2 μ s. So, for our case we need to use 88.05 MHz sweep frequency, which is $\frac{1}{4}$ of storage ring RF frequency. Synchro-scanning at $\frac{1}{4}$ RF with an RF light input frequency causes 2 out of 4 light impulses to be deflected out of image range (say bunch 1 & 3), and the other bunches to be scanned in the opposite direction (say, bunch 2 up- and bunch 4 down-wards). This aspect has no negative consequences for the Streak Camera's application or the interpretation of results. Synchroscan unit has trigger delay tuneup possibility with more than one period range, so we don't need external delay unit, but require that jitter of synchro signal better than 1 ps. That jitter is provided, for example, by frequency divider LJFD/H4 from Optronis [70].

3 other clock signals must be synchronized with readout trigger, with each other, and also with RF frequency. Readout trigger frequency is defined by dual time base extender unit, which allow to tune sweep time to horizontal electrodes within 100 ns to 100 ms range with maximum sweep frequency is 10 Hz. To register fill pattern of the full ring, sweep time should be set to $\sim 3.7 \mu$ s. These 3 trigger signals are not required to meet the same stringent jitter requirements as vertical electrodes, so all these functionalities can be unified within single self-made unit. This unit should generate trigger signal to readout camera with frequency of several Hz, receive storage ring RF frequency, divide it by 1296 (storage ring harmonic number), synchronize it with readout camera trigger, and generate 3 trigger signals with acceptable delays between them.

Streak Camera Equipment

The mutual repulsion of the photo-electrons in the same bunch can also cause non-negligible time dispersion (known as space-charge effects). To avoid this effect the number of photons in a given light pulse have to be kept below a certain level. But operating a streak camera at this level means that the statistical noise will impose a limitation on the Signal-to-Noise ratio of the measurement data. This flux level decreases exponentially with the pulse duration of the input signal and it means that the data quality (or S/N ratio) decreases strongly for single shot measurements of short light pulses. If the light source itself is repetitive and stable in phase then poor data quality can be improved by accumulation. However, unless a perfect synchronization between the input pulse and the streak camera's trigger exists, i.e. non-negligible jitter, the measurement results would be false.

Summing up all the above remarks, we can define required equipment for the streak camera within the bunch length measurement system:

- Set of mirrors, splitters and lenses to transmit light to streak camera
- Frequency divider of external RF frequency down to 88 MHz, or $\frac{1}{4}$ of RF frequency -



Optronis LJFD/H4

- Synchroscan sweep unit M10911-01
- Dual time base extender unit M10916-01
- Power supply
- Output optics A11695-11
- Mount table A11771-03
- Readout camera – ORCA-Flash4.0 V3
- Data analyzer

6.5 Halo Monitor

Beam halo measurements imply measurements of beam profiles with a very high dynamic range. Beam halo measurements in longitudinal plane is named ‘bunch purity’, and was presented early. Currently, we describe beam halo measurement in transverse vertical plane.

In particle accelerator beam experiments, background due to beam halo can mask the rare physics processes in the experiment detectors. Also, the detectors are often the most radiation sensitive components in the accelerator. The beam loss threshold enforced by the sensitivity of the experiments is often far below that imposed by the activation of machine components. The loss of <0.1‰ particles/bunch is sometimes already critical (e.g., can be harmful). Therefore, a beam halo monitor must be capable of measuring the transverse beam profile better than this. The required dynamic range for such a monitor should be of the order of 10^5 or even better.

Presented non-destructive halo monitor, developed in ESRF for EBS storage ring [71], is based on the transverse profile measurements of the X-ray synchrotron radiation after bending magnet, which is proportional to the population density of the electron’s beam. The system is measure only vertical profile of synchrotron radiation at far distance from the central core. To improve the dynamic range, central and lower part of the beam are attenuated by vertical absorber down to levels, comparable with the synchrotron radiation intensity of the upper part of the beam, which is not attenuated. Knowing the attenuation level of the absorber, we can determine the beam profile levels at far distance from the central core (up to 5-6 mm from the center) relative to the main beam amplitudes, thus increasing the dynamic range of the measurement system.

The block diagram of the measurement system is shown on Figure 44. Two horizontal and one vertical cooled absorbers are used to limit strength of X-Ray Synchrotron Radiation to the un-cooled 2 mm Aluminum window. The upper border of the vertical absorber should be positioned about 1 mm above the center of the beam, where level of the gaussian profile of the synchrotron radiation after 0.45 T bending magnet is about 10^{-9} lower than radiation intensity in the center of the beam. The thickness of the copper absorber and the additional tungsten absorber should be selected so that the radiation intensity at the center of the beam on the scintillator is comparable to the radiation intensity at the beam periphery, where the beam is attenuated only by a 2 mm Al window. Namely, for pure beams without a halo, the radiation intensity at the center of the beam should be approximately an order of magnitude higher than at the periphery, while when a halo appears, the radiation intensity at the beam periphery will increase. The synchrotron radiation is



registered by X-ray imager system consisted from 1mm thick Prelude scintillator, visual light optical system – mirrors and focusing double achromat lenses, and VCD Camera. This imager system should be placed inside lead shielding box to protect it from X-Ray synchrotron radiation.

Thus, from the measured beam profile along the vertical coordinate, knowing the intensity attenuation coefficient at the center of the synchrotron radiation and the spectral characteristic of the selected scintillator (LYSO – Cerium doped Lutetium based scintillation crystal Scintillation Material $Lu_{1.8}Y_{0.2}SiO_5:Ce$ 1 mm thickness from Saint-Gobain Crystals [72]), it is possible to calculate the ratio of the synchrotron radiation intensity at the center and at the periphery of the beam. And by calculating the areas under the radiation profile curve separately for the center and periphery of the beam, determine the halo level as the ratio of the current at a given distance from the center of the beam to the beam current.

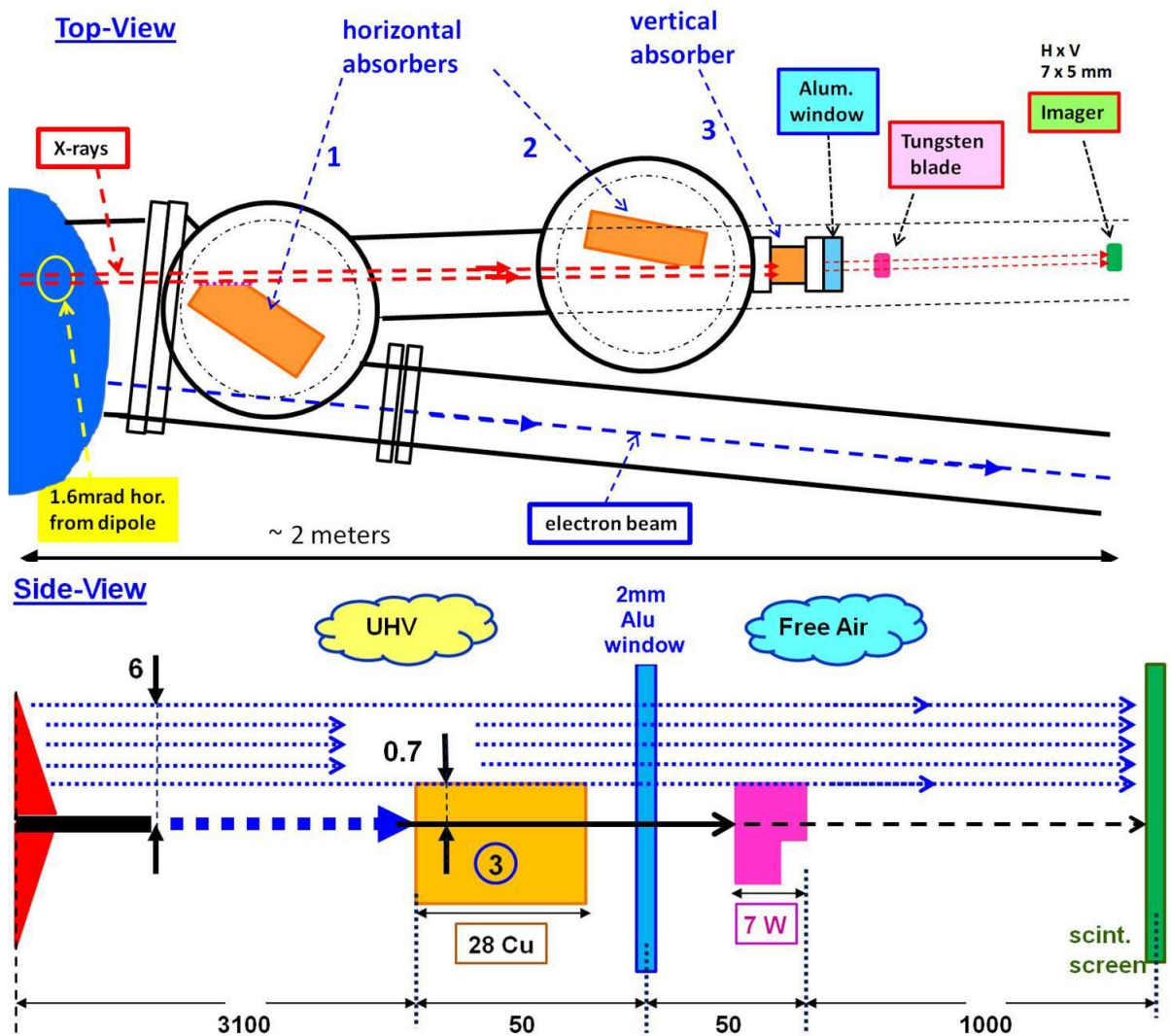


Figure 44. Halo Monitor.

By vertically moving tungsten absorber it is possible both to adjust peripheral intensity level by changing vertical position of absorber above copper vertical absorber, and to change attenuation on the center of the beam. For tungsten absorber with different thickness on different vertical coordinates, we can adjust beam attenuation more smoothly, which is important for measurement system calibration.



7 References

- [1] G.Kube, "Requirements for Beam Diagnostics & Measurement Principles," in *Proceedings of the 2018 CERN–Accelerator–School course on Beam Instrumentation*, Tuusula, (Finland), 2018.
- [2] CREMLIN+ TASK 4.1 2020 report: Lattice and systems for the main ring.
- [3] P. Raimondi, "Hybrid Multi Bend Achromat: From SuperB to EBS," in *Proceeding of IPAC 2017*, Copenhagen, Denmark, 2017.
- [4] S.M. Liuzzo et al., "USSR HMBA Storage Ring Lattice Options," in *Proceedings of IPAC2021*, Campinas, SP, Brasil, 2021.
- [5] L. Torino et al., "Overview on the Diagnostics for EBS-ESRF," in *Proceedings of IBIC 2019*, Malmo, Sweden, 2019.
- [6] DRAFT USSR RF report.
- [7] A. A. Nosych, U. Iriso, and J. Olle, "Electrostatic Finite- element Code to Study Geometrical Nonlinear Effects of BPMs in 2D," in *Proc. 4th Int. Beam Instrumentation Conf. (IBIC 15)*, Melbourne, Australia, 2005.
- [8] "Bergoz – FCT - Very fast non-destructive pulsed or CW beams observation," [Online]. Available: <https://www.bergoz.com/products/fct/>. [Accessed 16 01 2022].
- [9] "Bergoz – ICT & BCM-IHR-E - Beam charge measurement," [Online]. Available: <https://www.bergoz.com/products/ict/>. [Accessed 16 01 2022].
- [10] K. Unser, "Design and preliminary tests of a beam intensity monitor for LEP," in *Proceedings of the IEEE Particle Accelerator Conference*, Chicago, USA, 1989.
- [11] "Bergoz – NPCT - Non-destructive DC beam current measurement," [Online]. Available: <https://www.bergoz.com/products/npct/>. [Accessed 16 01 2022].
- [12] K. Unser, "The Parametric Current Transformer, a beam current monitor developed for LEP," in *Accelerator Instrumentation Workshop, AIP Proceedings No. 252*, Newport, 1991.
- [13] P. Forck, "Signal treatment of a stripline pick-up," in *Lecture Notes on Beam Instrumentation and Diagnostics*, CreateSpace Independent Publishing Platform, 2015, pp. 87-91.
- [14] M. Lonza, "Multi-bunch feedback systems," in *CERN Accelerator School: Course on Beam Diagnostics*, Geneva, CERN Yellow Reports: School Proceedings, 2009, p. 491.



- [15] Cyrille Thomas, Guenther Rehm, Ian Martin and Riccardo Bartolini, "X-ray pinhole camera resolution and emittance measurement," *Phys. Rev. ST Accel. Beams*, vol. 13, no. 022805, pp. 022805-1-11, 2010.
- [16] P. Elleaume, C. Fortgang, C. Penel and E. Tarazona, "Measuring Beam Sizes and Ultra-Small Electron Emittances Using an X-ray Pinhole Camera," *J. Synchrotron Rad.*, vol. 2, pp. 209-214, 1995.
- [17] L. Torino, U. Iriso, "Limitations and solutions of beam size measurements via interferometry at ALBA," in *Proceedings of 4th International Beam Instrumentation Conference*, Melbourne, Australia, 2015.
- [18] G. Kube, R. Fischer, K. Wittenburg, "Synchrotron Radiation Profile Monitor for the HERA Positron Beam," in *AIP Conference Proceedings*, 2004.
- [19] G. Kube, et al., "Detailed resolution studies of the synchrotron radiation profile monitor for the HERA electron beam," in *Proceedings of DIPAC 2005*, Lyon, France, 2005.
- [20] F. Ewald, "Beam Size Monitoring at the ESRF: Comparizon of different X-ray based techniques," in *Topical Workshop on Emittance Measurements for Light Sources and FELs*, Barseelona, 2018.
- [21] G. Kube, "Review of Sybchrotron Radiation Based Diagnostics for Transverse Profile Measurements," in *Proceedings of DIPAC 2007*, Venice, Italy, 2007.
- [22] "ochubar/SRW: Synchrotron Radiation Workshop," [Online]. Available: <https://github.com/ochubar/SRW>.
- [23] "Home Page of SPECTRA," [Online]. Available: <https://spectrax.org/spectra/>.
- [24] "RAY-UI: A user interface for RAY - Helmholtz-Zentrum Berlin (HZB)," [Online]. Available: https://www.helmholtz-berlin.de/forschung/oe/wi/optik-strahlrohre/arbeitsgebiete/ray_en.html.
- [25] "xop 2.4," [Online]. Available: <https://www.esrf.fr/Instrumentation/software/data-analysis/xop2.4>.
- [26] "oasys-kit/ShadowOui," [Online]. Available: <https://github.com/oasys-kit/ShadowOui>.
- [27] A. Hofmann, "The spectral distribution," in *The Physics of Synchrotron Radiation*, Cambridge, Cambridge University Press, 2004, p. 89.
- [28] Cyrille Thomas, Frederike Evalds, John Flanagan, "Large Aperture X-ray Monitors for Beam Profile Diagnostics," in *Proceedings of IBIC2013*, Oxford, UK, 2013.



- [29] N. Samadi, X. Shi, L. Dallin, and D. Chapman, "Source size measurement options for low-emittance light sources," *Phys. Rev. Accel. Beams*, vol. 23, no. 024801, pp. 024801-1-11, 2020.
- [30] J. W. Goodman, *Introduction to Fourier Optics*, New York: McGraw-Hill, 1996.
- [31] L.M. Bobb, A.F.D. Morgan, G. Rehm, "Performance Evaluation of Molybdenum Blades in an X-Ray Pinhole Camera," in *Proceedings of IBIC2016*, Barcelona, Spain, 2016.
- [32] L. Torino, U. Iriso, "Transverse beam profile reconstruction using synchrotron radiation interferometry," *Phys. Rev. Accel. Beams*, vol. 19, no. 122801, 2016.
- [33] A. Potylitsyn, L. Sukhikh, T. Gusvitskii, G. Kube, A. Novokshonov, "Image of the transverse bunch profile via coherent optical transition radiation," *Phys. Rev. Accel. Beams*, vol. 23, no. 042804, 2020.
- [34] A. H. Lumpkin, et al., "Optical techniques for electron-beam characterizations on the APS SASE FEL project," *Nucl. Instrum. Methods Phys. Res., vol. Sect. A*, no. 429, p. 336, 1999.
- [35] K. Fukami, et al., "Ejected beam emittance of the SPring-8 booster synchrotron," in *Proceedings of EPAC 2002*, Paris, France, 2002.
- [36] C. Thomas, et al., "Single shot transverse emittance measurement from OTR screens in a drift transport section," *JINST*, vol. 6, no. P07004, 2011.
- [37] Yu.A. Goponov, R.A. Shatokhin, K. Sumitani, Y. Takabayashi, I.E. Vnukov, "Diffracted transition radiation as a new diagnostic tool for relativistic electron beam emittance," *Nuclear Inst. and Methods in Physics Research*, vol. A 996, no. 165132, 2021.
- [38] A. Cianchi, et al., "Nonintercepting electron beam size monitor using optical diffraction radiation interference," *Phys. Rev. Accel. Beams*, vol. 14, no. 102803, 2011.
- [39] R.B. Fiorito, D.W. Rule, "Optical transition radiation beam emittance diagnostics," in *AIP Conference Proceedings 319*, 1994.
- [40] A.I. Novokshonov, A.P. Potylitsyn, G. Kube, "Two-Dimensional Synchrotron Radiation Interferometry at PETRA III," in *Proc. IPAC*, Copenhagen, Denmark, 2017.
- [41] D.Yu. Sergeeva., A.A. Tishchenko, M.N. Strikhanov, "UV and X-ray diffraction and transition radiation from charged particles bunches," *Nuclear Instruments and Methods in Physics Research*, vol. B, no. 309, p. 189, 2013.
- [42] A. A. Tishchenko, D. Yu. Sergeeva, "Incoherent Form Factor in Diffraction and Smith–Purcell Radiations," *JETP Letters*, vol. 110, p. 638–645, 2019.



- [43] D. I. Garaev, D. Yu. Sergeeva, A. A. Tishchenko, "Theory of Smith-Purcell radiation from a 2D array of small noninteracting particles," *Phys. Rev.*, vol. B 103, no. 075403, 2021.
- [44] D.Yu. Sergeeva, A.A. Tishchenko, M.N. Strikhanov, "Microscopic theory of Smith-Purcell radiation from 2D photonic crystal," *Nucl. Instr. and Methods*, vol. B 402, pp. 206-211, 2017.
- [45] D. Yu. Sergeeva, A. S. Aryshev, A. A. Tishchenko, K. E. Popov, N. Terunuma, J. Urakawa, "THz Smith–Purcell and grating transition radiation from metasurface: experiment and theory," *Optics Letters*, vol. 46, pp. 544-547, 2021.
- [46] D. I. Garaev, D. Yu. Sergeeva, A. A. Tishchenko, "Theory of Smith-Purcell radiation from a 2D array of small noninteracting particles," *Phys. Rev.*, vol. B 103, p. 075403, 2021.
- [47] D.I. Garaev, A.A. Tishchenko, D.Yu. Sergeeva, "Smith-Purcell radiation in prewave zone for diagnostics of relativistic electron beams, Abstracts of the XXVII Russian particle accelerator conference," in *RuPAC 2021*, 2021.
- [48] A.A. Tishchenko, D.Yu. Sergeeva, "Near-field resonances in photon emission via interaction of electrons with coupled nanoparticles," *Phys. Rev.*, vol. B 100, no. 235421, 2019.
- [49] P. Cherenkov, "Visible radiation produced by electrons moving in a medium with velocities exceeding that of light," *Phys. Rev.*, vol. 52, p. 378, 1939.
- [50] I. E. Tamm and I. M. Frank, "Coherent radiation of a fast electron in a medium," *Sov. Phys. Dokl.*, vol. 14, p. 107, 1937.
- [51] I. Tamm, "Radiation emitted by uniformly moving particles," *J. Phys.*, vol. 1, p. 439, 1939.
- [52] T. Kajita, "Nobel lecture: Discovery of atmospheric neutrino oscillations," *Rev. Mod. Phys.*, vol. 88, no. 030501, 2016.
- [53] M. Demarteau, R. Lipton, H. Nicholson, and I. Shipsey, "Particle and nuclear physics instrumentation and its broad connections," *Rev. Mod. Phys.*, vol. 88, no. 045007, 2016.
- [54] C. W. Fabjan and F. Gianotti, "Calorimetry for particle physics," *Rev. Mod. Phys.*, vol. 75, p. 1243, 2003.
- [55] [Online]. Available: <https://www.3ds.com/ru/produkty-i-uslugi/simulia/produkty/cst-studio-suite/>.
- [56] R. Kieffer, L. Bartnik, M. Bergamaschi et al., "Direct Observation of Incoherent Cherenkov Diffraction Radiation in the Visible Range," *Phys. Rev. Lett.*, vol. 121, no. 054802, 2018.
- [57] S. Kishimoto, "Bunch-purity measurements of synchrotron X-ray beams with an avalanche photodiode detector," *Nuclear Instruments and Methods in Physics Research*, vol. A, no. 351, pp.



- 554-558, 1994.
- [58] T. Obina et al, "Measurement of the longitudinal bunch structure in the Photon Factory positron storage ring with a photon counting method," *Nucl. Instrum. Methods*, vol.354, pp. 204-214, 1995.
- [59] T. Kasuga, H. Yonehara, M. Hasumoto and T. Kinoshita, *Jpn. J. Appl. Phys.*, vol. 28, p. 541, 1989.
- [60] Derenzo, W.W. Moses and S.E., *Nucl. Instr. and Meth.*, vol. A 291, p. 435, 1990.
- [61] "Si APD S12053-10 | Hamamatsu Photonics," [Online]. Available: <https://www.hamamatsu.com/eu/en/product/type/S12053-10/index.html>.
- [62] S. Sze, in *Physics of Semiconductor Devices (2nd. ed.)*, New York, Wiley, 1981, p. 45.
- [63] Alfred Q. R. Baron, Shunji Kishimoto, John Morse, Jean-Marie Rigal,, "Silicon avalanche photodiodes for direct detection of X-rays," *Journal of Synchrotron Radiation*, vol. 13, no. 2, pp. 131-142, 2006.
- [64] B. Joly, G.A. Naylor, "A high dynamic range bunch purity tool," in *Proceedings of DIPAC*, 2001.
- [65] A. Thompson et al., X-ray data booklet, DouglasEditors, 2001.
- [66] H. Franz et al., "Parasitic bunch measurement in e⁺/e⁻ storage rings," in *Proceedings of Sixth European Workshop on Beam Diagnostics and Instrumentation for Particle Accelerators, DIPAC03*, Mainz, 2003.
- [67] "PicoHarp 300 and PicoQuant Hybrid PMA," [Online]. Available: <https://www.picoquant.com/>.
- [68] "Guide to Streak Cameras," [Online]. Available: https://www.hamamatsu.com/resources/pdf/sys/SHSS0006E_STREAK.pdf.
- [69] "Universal streak camera | Hamamatsu Photonics," [Online]. Available: <https://www.hamamatsu.com/eu/en/product/photometry-systems/streak-camera/universal-streak-camera/index.html>.
- [70] G. Schiwietz, J.-G. Hwang, A. Jankowiak, M. Koopmans, M. Ries, "Bunch-resolved diagnostics for a future electron-storage ring," *Nuclear Inst. and Methods in Physics Research*, no. A 990, 2021.
- [71] B. Scheidt, "Non-Destructive Vertical Halo Monitor on the ESRF's 6GeV Electron Beam," in *Proceedings of IBIC2014*, Monterey, CA, USA, 2014.
- [72] "LYSO-Material-Data-Sheet," [Online]. Available: <https://www.crystals.saint-gobain.com/sites/hps-mac3-cma-crystals/files/2021-08/LYSO-Material-Data-Sheet.pdf>.





Addendum

Diag	s[m]
BPM_C04_01	2,14744
BLM_C04_1	4,01310
BPM_C04_02	6,78046
BPM_C04_03	7,81646
BPM_C04_04	10,89446
BPM_C04_05	13,23856
BPM_C04_06	14,34042
BPM_C04_07	16,68453
BLM_C04_2	17,61419
BPM_C04_08	19,76253
BPM_C04_09	20,79853
H_Scraper	20,79853
BLM_C04_3	22,67904
BLM_C04_4	24,58152
BPM_C04_10	24,92752
BPM_C05_01	30,23032
BLM_C05_1	30,28132
BLM_C05_2	32,06098
BPM_C05_02	34,35932
BPM_C05_03	35,39532
BPM_C05_04	38,47332
BPM_C05_05	40,81742
BPM_C05_06	41,91928
BPM_C05_07	44,26339
BLM_C05_3	45,19305
BPM_C05_08	47,34139
BPM_C05_09	48,37739
CT	48,37739
BLM_C05_4	50,25790
BPM_C05_10	52,50638
BPM_C06_01	57,80918
BLM_C06_1	57,86018
BLM_C06_2	59,63984
BPM_C06_02	61,93818
BPM_C06_03	62,97418
BPM_C06_04	66,05218
BPM_C06_05	68,39628
BPM_C06_06	69,49815
BPM_C06_07	71,84225
BLM_C06_3	72,77191
BPM_C06_08	74,92025
BPM_C06_09	75,95625

V_Scraper	75,95625
BLM_C06_4	77,83676
BPM_C06_10	80,08524
BPM_C07_01	85,38804
BLM_C07_1	85,43904
PINHOLE_ID07	86,48012
BLM_C07_2	87,21870
BPM_C07_02	89,51704
BPM_C07_03	90,55304
BPM_C07_04	93,63104
BPM_C07_05	95,97514
BPM_C07_06	97,07701
BPM_C07_07	99,42111
BLM_C07_3	100,35077
BPM_C07_08	102,49911
BPM_C07_09	103,53511
BeamKiller	103,53511
BLM_C07_4	105,41562
BPM_C07_10	107,66410
BPM_C08_01	112,96690
BLM_C08_1	113,01790
BLM_C08_2	114,79756
BPM_C08_02	117,09590
BPM_C08_03	118,13190
BPM_C08_04	121,20990
BPM_C08_05	123,55400
BPM_C08_06	124,65587
BPM_C08_07	126,99997
BLM_C08_3	127,92963
BPM_C08_08	130,07797
BPM_C08_09	131,11397
	131,11397
BLM_C08_4	132,99448
BPM_C08_10	135,24296
BPM_C09_01	140,54576
BLM_C09_1	140,59676
BLM_C09_2	142,37642
BPM_C09_02	144,67476
BPM_C09_03	145,71076
BPM_C09_04	148,78876
BPM_C09_05	151,13286
BPM_C09_06	152,23473
PINHOLE_D09	153,09256



BPM_C09_07	154,57883
BLM_C09_3	155,50849
BPM_C09_08	157,65683
BPM_C09_09	158,69283
HV_Kicker	158,69283
BLM_C09_4	160,57334
BPM_C09_10	162,82182
BPM_C10_01	168,12462
BLM_C10_1	168,17562
BLM_C10_2	169,95528
BPM_C10_02	172,25362
BPM_C10_03	173,28962
BPM_C10_04	176,36762
BPM_C10_05	178,71172
BPM_C10_06	179,81359
BPM_C10_07	182,15769
BLM_C10_3	183,08735
BPM_C10_08	185,23569
BPM_C10_09	186,27169
CT	186,27169
BLM_C10_4	188,15220
BPM_C10_10	190,40068
BPM_C11_01	195,70348
BLM_C11_1	195,75448
BLM_C11_2	197,53414
BPM_C11_02	199,83248
BPM_C11_03	200,86848
BPM_C11_04	203,94648
BPM_C11_05	206,29058
BPM_C11_06	207,39245
BPM_C11_07	209,73655
BLM_C11_3	210,66621
BPM_C11_08	212,81455
BPM_C11_09	213,85055
H_Scraper	213,85055
BLM_C11_4	215,73106
BPM_C11_10	217,97954
BPM_C12_01	223,28234
BLM_C12_1	223,33334
BLM_C12_2	225,11300
BPM_C12_02	227,41134
BPM_C12_03	228,44734
BPM_C12_04	231,52534
BPM_C12_05	233,86944
BPM_C12_06	234,97131
BPM_C12_07	237,31541
BLM_C12_3	238,24507
BPM_C12_08	240,39341

BPM_C12_09	241,42941
20-Button	241,42941
BLM_C12_4	243,30992
BPM_C12_10	245,55840
BPM_C13_01	250,86120
BLM_C13_1	250,91220
BLM_C13_2	252,69186
BPM_C13_02	254,99020
BPM_C13_03	256,02620
BPM_C13_04	259,10420
BPM_C13_05	261,44830
BPM_C13_06	262,55017
BPM_C13_07	264,89427
BLM_C13_3	265,82393
BPM_C13_08	267,97227
BPM_C13_09	269,00827
Collimator	269,00827
BLM_C13_4	270,88878
BPM_C13_10	273,13726
BPM_C14_01	278,44006
BLM_C14_1	278,49106
BLM_C14_2	280,27072
BPM_C14_02	282,56906
BPM_C14_03	283,60506
BPM_C14_04	286,68306
BPM_C14_05	289,02716
BPM_C14_06	290,12903
BPM_C14_07	292,47313
BLM_C14_3	293,40279
BPM_C14_08	295,55113
BPM_C14_09	296,58713
	296,58713
BLM_C14_4	298,46764
BPM_C14_10	300,71612
BPM_C15_01	306,01892
BLM_C15_1	306,06992
BLM_C15_2	307,84958
BPM_C15_02	310,14792
BPM_C15_03	311,18392
BPM_C15_04	314,26192
BPM_C15_05	316,60602
BPM_C15_06	317,70789
BPM_C15_07	320,05199
BLM_C15_3	320,98165
BPM_C15_08	323,12999
BPM_C15_09	324,16599
CT	324,16599
BLM_C15_4	326,04650



BPM_C15_10	328,29498
BPM_C16_01	333,59778
BLM_C16_1	333,64878
BLM_C16_2	335,42844
BPM_C16_02	337,72678
BPM_C16_03	338,76278
BPM_C16_04	341,84078
BPM_C16_05	344,18488
BPM_C16_06	345,28675
BPM_C16_07	347,63085
BLM_C16_3	348,56051
BPM_C16_08	350,70885
BPM_C16_09	351,74485
	351,74485
BLM_C16_4	353,62536
BPM_C16_10	355,87384
BPM_C17_01	361,17664
BLM_C17_1	361,22764
BLM_C17_2	363,00730
BPM_C17_02	365,30564
BPM_C17_03	366,34164
BPM_C17_04	369,41964
BPM_C17_05	371,76374
BPM_C17_06	372,86561
PINHOLE_D17	373,72344
BPM_C17_07	375,20971
BLM_C17_3	376,13937
BPM_C17_08	378,28771
BPM_C17_09	379,32371
	379,32371
BLM_C17_4	381,20422
BPM_C17_10	383,45270
BPM_C18_01	388,75550
BLM_C18_1	388,80650
BLM_C18_2	390,58616
BPM_C18_02	392,88450
BPM_C18_03	393,92050
BPM_C18_04	396,99850
BPM_C18_05	399,34260
BPM_C18_06	400,44447
BPM_C18_07	402,78857
BLM_C18_3	403,71823
BPM_C18_08	405,86657
BPM_C18_09	406,90257
	406,90257
BLM_C18_4	408,78308
BPM_C18_10	411,03156
BPM_C19_01	416,33436

BLM_C19_1	416,38536
BLM_C19_2	418,16502
BPM_C19_02	420,46336
BPM_C19_03	421,49936
BPM_C19_04	424,57736
BPM_C19_05	426,92146
BPM_C19_06	428,02333
BPM_C19_07	430,36743
BLM_C19_3	431,29709
BPM_C19_08	433,44543
BPM_C19_09	434,48143
	434,48143
BLM_C19_4	436,36194
BPM_C19_10	438,61043
BPM_C20_01	443,91323
BLM_C20_1	443,96423
BLM_C20_2	445,74388
BPM_C20_02	448,04222
BPM_C20_03	449,07822
BPM_C20_04	452,15622
BPM_C20_05	454,50032
BPM_C20_06	455,60219
BPM_C20_07	457,94629
BLM_C20_3	458,87595
BPM_C20_08	461,02429
BPM_C20_09	462,06029
	462,06029
BLM_C20_4	463,94080
BPM_C20_10	466,18929
BPM_C21_01	471,49209
BLM_C21_1	471,54309
BLM_C21_2	473,32274
BPM_C21_02	475,62108
BPM_C21_03	476,65708
BPM_C21_04	479,73508
BPM_C21_05	482,07918
BPM_C21_06	483,18105
BPM_C21_07	485,52515
BLM_C21_3	486,45481
BPM_C21_08	488,60315
BPM_C21_09	489,63915
	489,63915
BLM_C21_4	491,51966
BPM_C21_10	493,76815
BPM_C22_01	499,07095
BLM_C22_1	499,12195
BLM_C22_2	500,90160
BPM_C22_02	503,19994



BPM_C22_03	504,23594
BPM_C22_04	507,31394
BPM_C22_05	509,65804
BPM_C22_06	510,75991
BPM_C22_07	513,10401
BLM_C22_3	514,03367
BPM_C22_08	516,18201
BPM_C22_09	517,21801
	517,21801
BLM_C22_4	519,09852
BPM_C22_10	521,34701
BPM_C23_01	526,64981
BLM_C23_1	526,70081
BLM_C23_2	528,48046
BPM_C23_02	530,77880
BPM_C23_03	531,81480
BPM_C23_04	534,89280
BPM_C23_05	537,23690
BPM_C23_06	538,33877
BPM_C23_07	540,68287
BLM_C23_3	541,61253
BPM_C23_08	543,76087
BPM_C23_09	544,79687
	544,79687
BLM_C23_4	546,67738
BPM_C23_10	548,92587
BPM_C24_01	554,22867
BLM_C24_1	554,27967
BLM_C24_2	556,05932
BPM_C24_02	558,35766
BPM_C24_03	559,39366
BPM_C24_04	562,47166
BPM_C24_05	564,81576
BPM_C24_06	565,91763
BPM_C24_07	568,26173
BLM_C24_3	569,19139
BPM_C24_08	571,33973
BPM_C24_09	572,37573
Collimator	572,37573
BLM_C24_4	574,25624
BPM_C24_10	576,50473
BPM_C25_01	581,80753
BLM_C25_1	581,85853
PINHOLE_ID25	582,89960
BLM_C25_2	583,63818
BPM_C25_02	585,93652
BPM_C25_03	586,97252
BPM_C25_04	590,05052

BPM_C25_05	592,39462
BPM_C25_06	593,49649
BPM_C25_07	595,84059
BLM_C25_3	596,77025
BPM_C25_08	598,91859
BPM_C25_09	599,95459
	599,95459
BLM_C25_4	601,83510
BPM_C25_10	604,08359
BPM_C26_01	609,38639
BLM_C26_1	609,43739
BLM_C26_2	611,21704
BPM_C26_02	613,51538
BPM_C26_03	614,55138
BPM_C26_04	617,62938
BPM_C26_05	619,97348
BPM_C26_06	621,07535
BPM_C26_07	623,41945
BLM_C26_3	624,34911
BPM_C26_08	626,49745
BPM_C26_09	627,53345
Shaker	627,53345
BLM_C26_4	629,41396
BPM_C26_10	631,66245
BPM_C27_01	636,96525
BLM_C27_1	637,01625
BLM_C27_2	638,79590
BPM_C27_02	641,09424
BPM_C27_03	642,13024
BPM_C27_04	645,20824
BPM_C27_05	647,55234
BPM_C27_06	648,65421
PINHOLE_D27	649,51204
BPM_C27_07	650,99831
BLM_C27_3	651,92797
BPM_C27_08	654,07631
BPM_C27_09	655,11231
H_Stripline	655,11231
BLM_C27_4	656,99282
BPM_C27_10	659,24131
BPM_C28_01	664,54411
BLM_C28_1	664,59511
BLM_C28_2	666,37476
BPM_C28_02	668,67310
BPM_C28_03	669,70910
BPM_C28_04	672,78710
BPM_C28_05	675,13120
BPM_C28_06	676,23307



BPM_C28_07	678,57717
BLM_C28_3	679,50683
BPM_C28_08	681,65517
BPM_C28_09	682,69117
H_Stripline	682,69117
BLM_C28_4	684,57168
BPM_C28_10	686,82017
BPM_C29_01	692,12297
BLM_C29_1	692,17397
BLM_C29_2	693,95362
BPM_C29_02	696,25196
BPM_C29_03	697,28796
BPM_C29_04	700,36596
BPM_C29_05	702,71006
BPM_C29_06	703,81193
BPM_C29_07	706,15603
BLM_C29_3	707,08569
BPM_C29_08	709,23403
BPM_C29_09	710,27003
V_Stripline	710,27003
BLM_C29_4	712,15054
BPM_C29_10	714,39903
BPM_C30_01	719,70183
BLM_C30_1	719,75283
BLM_C30_2	721,53248
BPM_C30_02	723,83082
BPM_C30_03	724,86682
BPM_C30_04	727,94482
BPM_C30_05	730,28892
BPM_C30_06	731,39079
BPM_C30_07	733,73489
BLM_C30_3	734,66455
BPM_C30_08	736,81289
BPM_C30_09	737,84889
H_Stripline	737,84889
BLM_C30_4	739,72940
BPM_C30_10	741,97789
BPM_C31_01	747,28069
BLM_C31_1	747,33169
BLM_C31_2	749,11134
BPM_C31_02	751,40968
BPM_C31_03	752,44568
BPM_C31_04	755,52368
BPM_C31_05	757,86778
BPM_C31_06	758,96965
BPM_C31_07	761,31375
BLM_C31_3	762,24341
BPM_C31_08	764,39175

BPM_C31_09	765,42775
V_Stripline	765,42775
BLM_C31_4	767,30826
BPM_C31_10	769,55675
BPM_C32_01	774,85955
BLM_C32_1	774,91055
BLM_C32_2	776,69020
BPM_C32_02	778,98854
BPM_C32_03	780,02454
BPM_C32_04	783,10254
BPM_C32_05	785,44664
BPM_C32_06	786,54851
BPM_C32_07	788,89261
BLM_C32_3	789,82227
BPM_C32_08	791,97061
BPM_C32_09	793,00661
	793,00661
BLM_C32_4	794,88712
BPM_C32_10	797,13561
BPM_C33_01	802,43841
BLM_C33_1	802,48941
BLM_C33_2	804,26906
BPM_C33_02	806,56740
BPM_C33_03	807,60340
BPM_C33_04	810,68140
BPM_C33_05	813,02551
BPM_C33_06	814,12737
BPM_C33_07	816,47147
BLM_C33_3	817,40113
BPM_C33_08	819,54947
BPM_C33_09	820,58547
Shaker	820,58547
BLM_C33_4	822,46598
BPM_C33_10	824,71447
BPM_C34_01	830,01727
BLM_C34_1	830,06827
BLM_C34_2	831,84792
BPM_C34_02	834,14626
BPM_C34_03	835,18226
BPM_C34_04	838,26026
BPM_C34_05	840,60437
BPM_C34_06	841,70623
BPM_C34_07	844,05033
BLM_C34_3	844,97999
BPM_C34_08	847,12833
BPM_C34_09	848,16433
	848,16433
BLM_C34_4	850,04484



BPM_C34_10	852,29333
BPM_C35_01	857,59613
BLM_C35_1	857,64713
BLM_C35_2	859,42678
BPM_C35_02	861,72512
BPM_C35_03	862,76112
BPM_C35_04	865,83912
BPM_C35_05	868,18323
BPM_C35_06	869,28509
BPM_C35_07	871,62919
BLM_C35_3	872,55885
BPM_C35_08	874,70719
BPM_C35_09	875,74319
	875,74319
BLM_C35_4	877,62370
BPM_C35_10	879,87219
BPM_C36_01	885,17499
BLM_C36_1	885,22599
BLM_C36_2	887,00564
BPM_C36_02	889,30398
BPM_C36_03	890,33998
BPM_C36_04	893,41798
BPM_C36_05	895,76209
BPM_C36_06	896,86395
BPM_C36_07	899,20805
BLM_C36_3	900,13771
BPM_C36_08	902,28605
BPM_C36_09	903,32205
	903,32205
BLM_C36_4	905,20256
BPM_C36_10	907,45105
BPM_C37_01	912,75385
BLM_C37_1	912,80485
BLM_C37_2	914,58450
BPM_C37_02	916,88284
BPM_C37_03	917,91884
BPM_C37_04	920,99684
BPM_C37_05	923,34095
BPM_C37_06	924,44281
BPM_C37_07	926,78691
BLM_C37_3	927,71657
BPM_C37_08	929,86491
BPM_C37_09	930,90091
	930,90091
BLM_C37_4	932,78142
BPM_C37_10	935,02991
BPM_C38_01	940,33271
BLM_C38_1	940,38371

BLM_C38_2	942,16336
BPM_C38_02	944,46170
BPM_C38_03	945,49770
BPM_C38_04	948,57570
BPM_C38_05	950,91981
BPM_C38_06	952,02167
BPM_C38_07	954,36577
BLM_C38_3	955,29543
BPM_C38_08	957,44377
BPM_C38_09	958,47977
	958,47977
BLM_C38_4	960,36028
BPM_C38_10	962,60877
BPM_C39_01	967,91157
BLM_C39_1	967,96257
BLM_C39_2	969,74222
BPM_C39_02	972,04056
BPM_C39_03	973,07656
BPM_C39_04	976,15456
BPM_C39_05	978,49867
BPM_C39_06	979,60053
BPM_C39_07	981,94463
BLM_C39_3	982,87429
BPM_C39_08	985,02263
BPM_C39_09	986,05863
	986,05863
BLM_C39_4	987,93914
BPM_C39_10	990,18763
BPM_C40_01	995,49043
BLM_C40_1	995,54143
BLM_C40_2	997,32108
BPM_C40_02	999,61942
BPM_C40_03	1000,65542
BPM_C40_04	1003,73342
BPM_C40_05	1006,07753
BPM_C40_06	1007,17939
BPM_C40_07	1009,52349
BLM_C40_3	1010,45315
BPM_C40_08	1012,60149
BPM_C40_09	1013,63749
	1013,63749
BLM_C40_4	1015,51800
BPM_C40_10	1017,76649
BPM_C01_01	1023,06929
BLM_C01_1	1023,12029
BLM_C01_2	1024,89994
BPM_C01_02	1027,19828
BPM_C01_03	1028,23428



BPM_C01_04	1031,31228
BPM_C01_05	1033,65639
BPM_C01_06	1034,75825
BPM_C01_07	1037,10235
BLM_C01_3	1038,03201
BPM_C01_08	1040,18035
BPM_C01_09	1041,21635
	1041,21635
BLM_C01_4	1043,09686
BPM_C01_10	1045,34535
BPM_C02_01	1050,64815
BLM_C02_1	1050,69915
BLM_C02_2	1052,47880
BPM_C02_02	1054,77714
BPM_C02_03	1055,81314
BPM_C02_04	1058,89114
BPM_C02_05	1061,23525
BPM_C02_06	1062,33711
BPM_C02_07	1064,68121
BLM_C02_3	1065,61087
BPM_C02_08	1067,75921
BPM_C02_09	1068,79521
	1068,79521
BLM_C02_4	1070,67572
BPM_C02_10	1072,92421
BPM_C03_01	1078,22701
BLM_C03_1	1078,27801
BLM_C03_2	1080,05766
BPM_C03_02	1082,35600
BPM_C03_03	1083,39200
BPM_C03_04	1086,47000
BPM_C03_05	1088,81411
BPM_C03_06	1089,91597
BPM_C03_07	1092,26007
BLM_C03_3	1093,18973
BPM_C03_08	1095,33807
BPM_C03_09	1096,37407
	1096,83907
BLM_C03_4	1098,72360
BPM_C03_10	1101,00709

